AALBORG UNIVERSITY

Adaptive frequency regulation strategy in multi-area microgrids including renewable energy and electric vehicles supported by virtual inertia

Abubakr , Hussein; Mohamed, Tarek Hassan; Hussein, Mahmoud M.; Guerrero, Josep M.; Tinajero, Gibran David Agundis

Adaptive frequency regulation strategy in multi-area microgrids including renewable energy and electric vehicles supported by virtual inertia

Hussein Abubakr[1,2*], Tarek Hassan Mohamed[1], Mahmoud M. Hussein[1], Josep M. Guerrero[2], Gibran Agundis-Tinajero[2].

[1]*Department of Electrical Engineering, Faculty of Energy Engineering, Aswan University, Aswan 81528, Egypt.*
[2]*Center for Research on Microgrids (CROM), Department of Energy Technology, Aalborg University, Aalborg, Denmark.*

*Corresponding author: Tel.:+201151181810
Email address: husseinabubakr@energy.aswu.edu.eg

ABSTRACT With the increased level of penetration of distributed generators (DGs), renewable energy sources (RESs) in microgrids (µGs), the impact of damping, and low inertia effect on the grid stability increase in the situation of uncertainties. This leads to some important issues that happened in the power systems such as power fluctuaCVtions due to the variable nature of RESs, frequency regulation degradation, voltage rise, and excessive supply due to full DGs generation in the grid electricity. A solution to improve the stability is to provide inertia virtually by virtual synchronous generators (VSGs) that can be created using an appropriate control mechanism. Therefore, to overcome the aforementioned challenges, a robust control strategy should be applied. In this study, a new adaptive control technique for on-line tuning the integral controllers' gains for power charging/discharging of plug-in electric vehicles (EVs) has been proposed using Harris hawks optimization (HHO) based Balloon Effect (BE) supported by a virtual inertia controller considering high-level penetration of RESs in islanded and interconnected µGs. The main target is to regulate the suggested µG frequency powered by a PV power source and a diesel generator in the presence of random load variations and flexible loads for enhancing system robustness and validity in face of parametric uncertainties and disturbances. The time delay caused by the communication process between the area and the control center is considered for the interconnected µGs dynamic model. The discussion and analysis of the results show that the suggested control strategy has a better performance on frequency regulation, and maintaining the stability of the µG system as compared to another powerful controller called coefficient diagram method (CDM) in presence/absence of the virtual inertia control loop.

KEYWORDS *Virtual inertia control, renewable energy sources (RESs), plug-in electric vehicle (PEV), adaptive control, Harris hawks optimization (HHO), micro-grid (µG).*

1. INTRODUCTION

In recent years, a huge amount of generation from RESs such as wind power and photovoltaic has being predicted to be established into the power systems according to the global warming countermeasures and energy security.

Frequency stability was secured by the large rotational inertia of synchronous machines in power systems due to its relieve various disturbances. The excessive growth of dispersed generation on a small-scale will lead to the decrease of the power system inertia constant, leading to instability and massive blackout in the grid [1]. A promising solution towards stabilizing such grids is to emulate the behavior of synchronous generator virtually into µGs for improving the system inertia, stability, and resiliency. For this purpose, VSG imitates the prime movers activity (inertia characteristics) [2,

3], moreover, provides a basis for maintaining the share of DGs in the µG without sacrificing its stability and flexibility.

A virtual inertia for DGs/RESs was established by using a short-term energy storage with a power electronics inverter/converter and a suitable control mechanism. These mechanisms were known as a virtual synchronous generator (VSG) or virtual synchronous machine (VISMA) [2-4]. The concept of the VSG is initially relied on reproducing the dynamic characteristics of a real synchronous generator (SG) for DG/RES units based on the power electronics, in order to inherit the SG merits in enhancing stability. The principle of VSG can be applied either to a single DG, or to a group of DGs. The first application may be more suitable for DGs individual proprietors, while the second application is more economical and simpler to control from point of view of the network operator [2].

Over the past few years, various control techniques were implemented based on the virtual inertia control to make strides in the µGs frequency stability [4–7]. A derivative controller-based virtual inertia is recommended to upgrade the frequency stability of the interconnected grid in [4]. A fuzzy logic control is proposed to implement a virtual inertial control to support island µGs frequency stability in [5, 6]. In [7], a robust H-infinity method based virtual inertia is proposed for analysis of islanded µG frequency stability considering high level of the RESs. In [8], a predictive model control (MPC) is proposed for a virtual inertial control application to counteract the high penetration level of RES in µG.

In [9], the virtual inertia control is applied based on a method of estimating frequency response to improve the system stability by penetrating high wind power. The proportional–integral–derivative (PID) or proportional–integral (PI) controller is considered one of the most common types of studying the frequency control issue because it has many benefits such as low cost and simplicity [10]. Additionally, it provides a trustworthy performance regardless of the disturbances and system parameters variation (i.e. system uncertainties) [11]. In [12], a coordinated control parameter set relies on a virtual inertia control for DFIG wind farms to guarantee both the stability of frequency and small-signal in µGs.

Based on the above control approaches, the uncertainty combinations were not designed and considered in either renewable power generators or load demand; however, a few research studies were undertaken on uncertainties in renewable resources for renewable power systems [13, 14]. The control strategy of virtual inertia is based on the rate of change of frequency (RoCoF) which calculates the deviation of system frequency to add an additional active power to the set-point, thus, this concept simulates the inertia properly, which contributes to the total inertia of the µG, enhancing transient frequency stability [15, 16].

One powerful control strategy involving CDM was introduced in [17, 18]. Essentially, CDM is an algebraic approach applied to a polynomial loop in the parameter space, such a special schematic diagram called coefficient diagram, which is used as the vehicle to carry the necessary design information and as the criteria of good design [19].

The technological challenges of PEVs relevant to energy storage system are described in [20, 21]. There were a number of probabilistic charging models, which involved calculations of random variables associated with PV outputs, EV and grid loads to generate probability density functions [22, 23].

Recently, the increase of variable load demands and utilization of renewable sources is leading to system frequency fluctuations. This problem pushed the researchers to focus on the benefits of installing the EVs in µGs as flexible loads [24]. In [25, 26], EVs are installed in residential areas for frequency control in the smart µG system as a controllable load. Additionally, integrating an EV with a virtual power plant can help in solving the aforementioned issues [27].

Some attempts have been made to implement optimization techniques to adjust control parameters due to their ability to address uncertainties and disturbances, and the participation of optimization techniques was appeared in many research papers as presented in [28-30]. Additionally, standard PI-LFCs that tuned off-line were used by optimization methods such as in [31, 32]. One solution to the complexity of the two-part adaptive load frequency control (LFC) is applying soft computing technique to optimize the LFC parameters directly [33-37].

On the other hand, a meta-heuristic optimization method called HHO [38] was used to determine the optimal value of the integral controller that controls the flexible loads according to system dynamics. HHO has more benefits, such as the ease of use, high speed convergence, less time calculation required, less depending on the set of initial values, does not need to tune its parameters unlike other heuristic algorithms during the computations, and solving the constrained/unconstrained optimization problems which makes it more powerful as shown in [26, 36, 37].

One of the weakness point of the classic HHO application in the adaptive control problem can be expressed as follows: according to the nominal transfer function of the plant considering no load disturbance, the objective function was designed. Therefore, poor performance may occur at the moment of load disturbance, variations of system parameters.

BE which is presented in [39, 40] was designed to make the optimizer more sensitive to the variations that affect the system, such as load variations and changes in the system parameters. It represents the effect of the system changes in the on-time system open loop transfer function, which is similar to the effect of air on balloon size. In addition, BE has designed to enable the HHO to work individually as an adaptive controller to tune the PID controller.

For the aforementioned reasons, this paper proposes a new adaptive control strategy for plug-in EVs in an islanded single area and interconnected two area µGs for on-line tuning the integral controller's gains of EVs by using the modified HHO based BE supported by virtual inertia controller. The suggested system is examined through the effect of frequency deviations and power fluctuations resulted from both random demand loads and RESs with the integration of the EVs. Digital simulation results have confirmed that the suggested strategy can be implemented effectively for LFC applications.

The main contribution of this research is to design a new appropriate control mechanism for PEVs for the incorporation of frequency control in presence of RESs uncertainties and virtual inertia (as an auxiliary control loop) to guarantee an evasion of system instability, and diminish the impacts of system issues such as load disturbance and parameters variation. We also provide a novel solution to enhance the power and frequency deviations for islanded single area and interconnected multi-area µGs using adaptive control strategy (HHO based BE + virtual inertia) for on-line tuning the controller's gains of PEVs. The concept of applied BE is to increase the interactivity and sensitivity of the optimizer (HHO) with the on-line system issues.

About the possibility of a real world implementation of the proposed method: it has been applied for electrical system

applications in [40, 41] for tuning the gains of PID controller for LFC and the position control of a cart driven by an armature-controlled DC motor.

2. PROBLEM DESCRIPTION

Since the power generation from RESs is variable, it leads to more fluctuations in power flow and frequency in the μG, which greatly affect the operation of the power system. Therefore, the high penetration of RESs makes the situation in μG worse due to low inertia; thus, creating a difficulty in stabilizing system frequency and voltage, which leads to weakening μG resiliency and stability. Moreover, random changes in the demand for load power caused a poor response to the common coupling voltage point and the transfer of active and reactive powers. As a result, sharp deviations that happened to system frequency have a negative impact on the control performance parameters in presence of high RESs power fluctuations and this will cause energizing of under/over-frequency relay and disconnect some loads. Therefore, a new coordination for stability issues has become a center of interest, especially for power system researchers.

3. SYSTEM CONFIGURATION

3.1. Structure of single area μG

The μG is a small power system, containing DG units, energy storage systems, and domestic loads. μG is distributed through low-voltage distribution systems and the electric power is generated mainly by DGs such as photovoltaic (PV), wind turbines (WT), hydro units, fuel cells etc. This research focuses on the isolated μG (base of 20 MW), which includes 17 MW of random loads, 20 MW of non-reheated turbine power plant, 6 MW from the solar array, and 11.9 MW of electric vehicle units (2.38 for each unit) as shown in Fig. 1.

In this study, the impacts of physical constraints such as the power plant generation rate constraints (GRC) and the speed governor's dead band are considered when modelling the actual islanded μG. GRC limits the rate of the resulting power generation, which is given as 0.2 p.u. MW/min for the non-reheat μG. In this paper, the power variance of RESs such as PV solar power (ΔP_{PV}), and load power (ΔP_L) are considered as disturbance signals. Figure 2 shows the studied μG dynamic model. The nominal parameters values for the μG are given in Table 1.
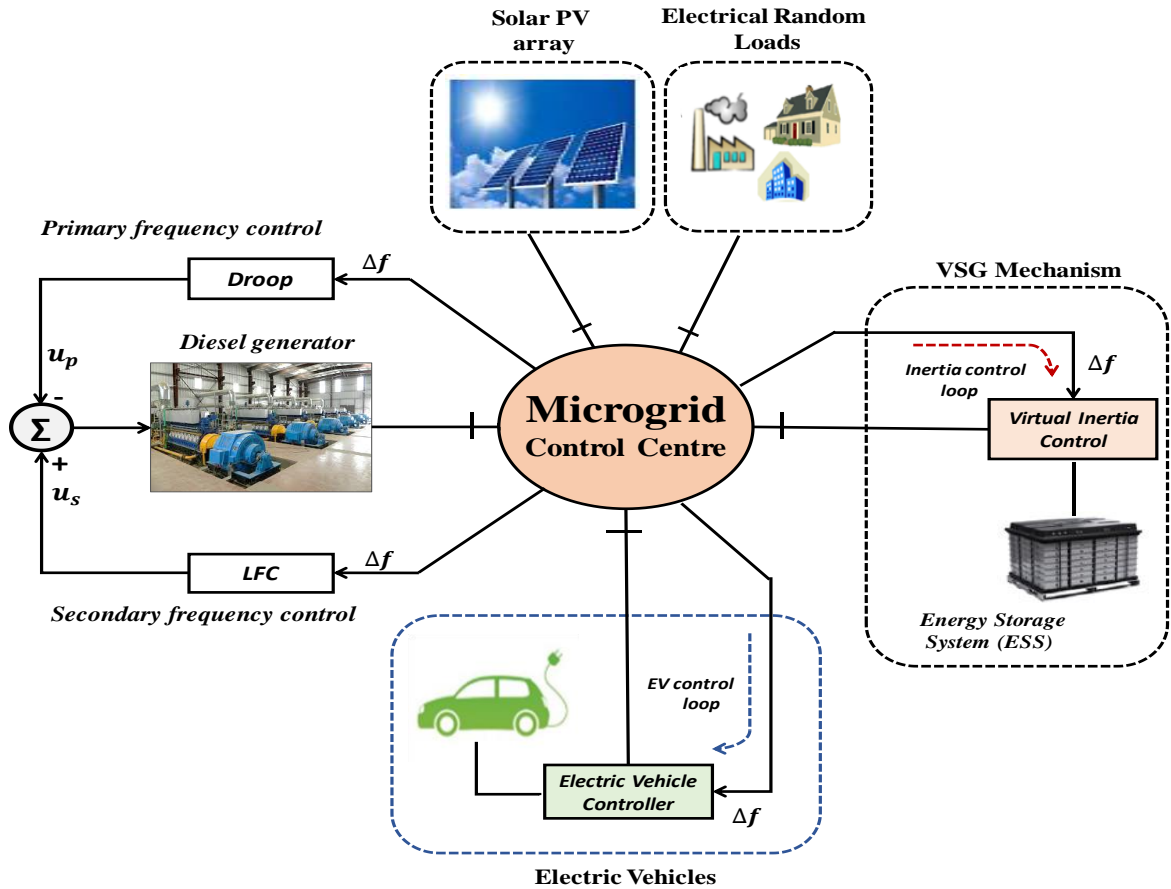

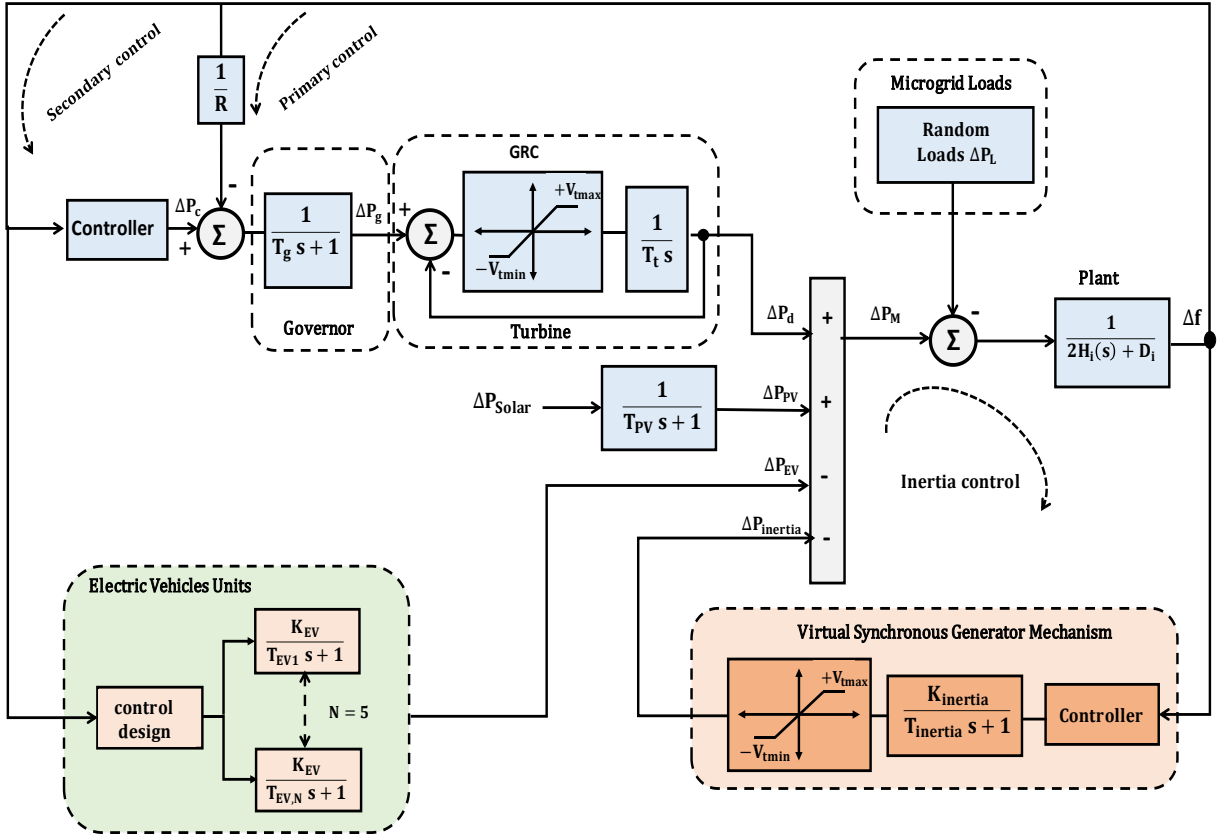**Fig. 1.** Construction of single area μG.

Fig. 2. Block diagram of the studied μG.

Table 1 Dynamic parameters of the islanded single area μG.

Parameter	D (pu/Hz)	H (pu.sec)	R (Hz/pu)	Tg (sec)	Tt (sec)	$T_{inertia}$ (sec)	$K_{inertia}$	KP	TEV (sec)	KEV	GRC (p.u.MW/min)
Value	0.12	0.10	2.40	0.10	0.40	10.0	1.0	2.581	0.28	1.0	20%

3.2 Virtual inertia control for μGs

The RESs can have major effects on system inertia (H) when its penetration level increases. Whereas, RESs exchange the power to the μGs through power electronic devices (i.e. inverters/ converters). RESs based power converter interfaces are stationary devices without any rotating mass so that the associated inertia constant is roughly zero [42]. Hence, the system's total inertia will be reduced along with an increase in the RESs penetration level, which increases the system's frequency deviation. To work around this issue, virtual inertia control has been applied. The prime mover activity is mimicked to support the islanded μG frequency stability [8]. Therefore, the islanded μGs inertia response induced by RESs can be compensated by adding active power to the set point, which is simulated by the virtual inertia control block as shown in Fig. 3.

The rate-of-change-of-frequency (RoCoF) function is used for many applications such as quick load shedding, to accelerate the operation time in over/under-frequency situations and to detect the grid loss. Therefore, the virtual inertia control strategy relies on RoCoF that calculates Δf to add a compensation active power to set point of the islanded μG during high-level RESs penetration and emergencies [7].

In addition, the prediction error of real-time using a relatively small timescale of minute will not affect frequency regulation [43]. Therefore, in the default virtual inertia model, the effect of frequency changes for output power limits is addressed as shown in Fig. 3.

RoCoF is calculated using the derivative control, which is the main concept of the virtual inertia control as:
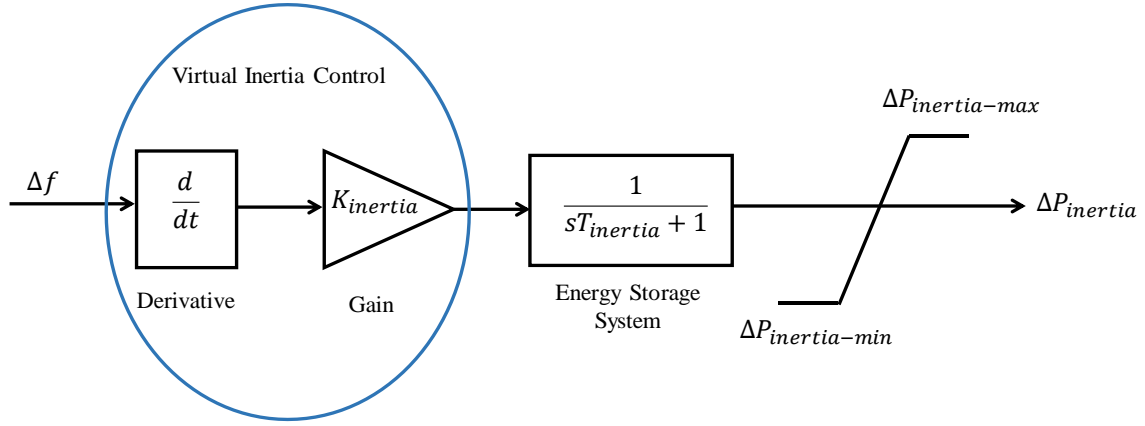
$$RoCoF = \left[\frac{d(\Delta f)}{dt}\right] \quad (1)$$

4

Fig. 3. Model of VSG.

.

Where the proposed control strategy supported by virtual inertia gives the desired power to the µG during the deviation of frequency when the RESs are penetrated highly as follows [7, 44]:

$$\Delta P_{inertia} = \frac{K_{inertia}}{sT_{inertia} + 1} \left[\frac{d(\Delta f)}{dt} \right] \tag{2}$$

Where, $T_{inertia}$ is the virtual inertia time constant to emulate the dynamic control of the energy storage system in the islanded µG, and $K_{inertia}$ is the gain of virtual inertia control in the islanded µG. The criteria for selecting these two parameters are related to the stability of the µG and the required response in dynamics. These parameters are indicated in Table 1.

3.3 Electric vehicle aggregator EVA controllable capacity

Due to transfers between charging and discharging state during the frequency regulation (FR) process, EVs' battery will be deteriorated. Regarding to [45], the state controlling of charging-discharging EV individuals can be solved by dividing the EVs in the FR service group into charging-discharging group. After completion of the switching process as described in [45] is over, the charging-discharging times TIME$_{i,j}$ shall be increased by one time as follows:

$$TIME_{i,j} = \begin{cases} TIME_{i,j-1} & P_{i,j-1}P_{i,j} \geq 0 \\ TIME_{i,j-1} + 1 & P_{i,j-1}P_{i,j} < 0 \end{cases} \tag{3}$$

3.3.1 Real-time prediction of EVA controllable capacity

At time j + 1, the EVA controllable capacity for up/down-regulation is obtained from real-time prediction at time j. The FR plan was violated by EVs users due to their schism from the grid at the declared time period, resulting in an inaccurate forecast of controlled power.

The concept of credibility ρ_i was introduced into the calculation of controllable capacity prediction to resolve the previous issue [46] and is defined as follows:

$$\rho_i = T_i^a \Big/ T_i^d = \begin{cases} 1 & \rho_{up \leq \bar{T}_i^a / \bar{T}_i^d} \\ \bar{T}_i^a \Big/ \bar{T}_i^d & \rho_{down \leq \bar{T}_i^a / \bar{T}_i^d < \rho_{up}} \\ 0 & \rho_{down > \bar{T}_i^a / \bar{T}_i^d} \end{cases} \tag{4}$$

When $\rho_i > \rho_{up}$, the EV is considered to be high reliable (high credibility), thus the value of ρ_i is set to 1 (the predictive controllable capacity of EVA will be fully integrated); if the $\rho_i < \rho_{down}$, the EV is considered to be non-reliable, thus the value of ρ_i is set to 0.

At time j, the predictive controllable capacity R_{j+1} at time j + 1 is shown as follows:

$$R_{j+1}^{up} = \sum_{i=1}^{N_i^{dc}} (m_i, \rho_i) \tag{5}$$

$$R_{j+1}^{down} = \sum_{i=1}^{N_i^c} (-m_i, \rho_i) \tag{6}$$

$$R_{j+1} = \begin{cases} R_{j+1}^{up} & \Delta f < 0 \\ R_{j+1}^{down} & \Delta f > 0 \\ 0 & \Delta f = 0 \end{cases} \tag{7}$$

In summary, as Eq. 7, the FR output power P_{j+1} of EVA at time j + 1 is shown as follows:

$$P_{j+1} = \begin{cases} P_{j+1}^{dc} & \Delta f < 0 \\ P_{j+1}^c & \Delta f > 0 \\ 0 & \Delta f = 0 \end{cases} \tag{8}$$

5

4. MATHEMATICAL MODEL OF THE PROPOSED MICROGRID SYSTEM

This section depicts the state-space equations from the proposed islanded µG at Fig. 2 considering high RESs penetrations. The islanded µG frequency deviation Δf under the effect of RESs penetration, the primary and secondary control can be obtained as:

$$\dot{\Delta f} = \left(\frac{1}{2H}\right)\left(\Delta P_d + \Delta P_g \pm \Delta P_{Inertia} - \Delta P_{EV} - \Delta P_L\right) - \left(\frac{D}{2H}\right).\Delta f \quad (9)$$

$$\dot{\Delta P_d} = -\left(\frac{1}{T_t}\right).\Delta P_d + \left(\frac{1}{T_t}\right).\Delta P_g \quad (10)$$

$$\dot{\Delta P_g} = -\left(\frac{1}{RT_g}\right).\Delta f - \left(\frac{1}{T_g}\right).\Delta P_g + \left(\frac{1}{T_g}\right).\Delta P_c \quad (11)$$

$$\dot{\Delta P_{PV}} = -\left(\frac{1}{T_{PV}}\right).\Delta P_{PV} + \left(\frac{1}{T_{PV}}\right).\Delta P_{Solar} \quad (12)$$

$$\dot{\Delta P_{EV}} = -\left(\frac{1}{T_{EV}}\right).\Delta P_{EV} + \left(\frac{K_{EV}}{T_{EV}}\right).\dot{\Delta f} \quad (13)$$

$$\dot{\Delta P_{Inertia}} = -\left(\frac{1}{T_{Int}}\right).\Delta P_{Inertia} + \left(\frac{K_{Int}}{T_{Int}}\right).\dot{\Delta f} \quad (14)$$

The studied µG dynamic equations can be extracted in the state variable form as follows:

$$\dot{X} = AX + BU + EW \quad (15)$$

$$Y = CX + DU + FW \quad (16)$$

$$\dot{X} = \begin{vmatrix} \frac{-D}{2H} & 0 & \frac{1}{2H} & \frac{1}{2H} & \frac{1}{2H} & \frac{1}{2H} \\ \frac{-1}{RT_g} & \frac{-1}{T_g} & 0 & 0 & 0 & 0 \\ 0 & \frac{1}{T_t} & \frac{-1}{T_t} & 0 & 0 & 0 \\ 0 & 0 & 0 & \frac{-1}{T_{PV}} & 0 & 0 \\ \frac{K_{EV}*D}{T_{EV}*2H} & 0 & \frac{K_{EV}}{T_{EV}*2H} & \frac{K_{EV}}{T_{EV}*2H} & \frac{K_{EV}}{T_{EV}*2H} & \left(\frac{K_{EV}}{T_{EV}*2H} - \frac{1}{T_{EV}}\right) \\ \frac{K_{Int}*D}{T_{Int}*2H} & 0 & \frac{K_{Int}}{T_{Int}*2H} & \frac{K_{Int}}{T_{Int}*2H} & \frac{K_{Int}}{T_{Int}*2H} & \left(\frac{K_{Int}}{T_{Int}*2H} - \frac{1}{T_{Int}}\right) \end{vmatrix} X$$

$$\begin{vmatrix} \Delta f \\ \Delta P_g \\ \Delta P_d \\ \Delta P_{PV} \\ \Delta P_{EV} \\ \Delta P_{Inertia} \end{vmatrix} + \begin{vmatrix} 0 \\ \frac{1}{T_g} \\ 0 \\ 0 \\ 0 \\ 0 \end{vmatrix} X |\Delta P_c| + \begin{vmatrix} 0 & \frac{1}{2H} \\ 0 & 0 \\ 0 & 0 \\ \frac{1}{T_{PV}} & 0 \\ 0 & \frac{K_{EV}}{T_{EV}*2H} \\ 0 & \frac{K_{Int}}{T_{Int}*2H} \end{vmatrix} X$$

$$\begin{vmatrix} \Delta P_{Solar} \\ \Delta P_L \end{vmatrix} \quad (17)$$

$$Y = |\; 1 \quad 0 \quad 0 \quad 0 \quad 0 \quad 0\;| \; x \begin{vmatrix} \Delta f \\ \Delta P_g \\ \Delta P_d \\ \Delta P_{PV} \\ \Delta P_{EV} \\ \Delta P_{Inertia} \end{vmatrix} + |\; 0 \quad 0\;| \; x$$

$$\begin{vmatrix} \Delta P_{Solar} \\ \Delta P_L \end{vmatrix} + |\; 0\;| \; x \; | \Delta P_c | \quad (18)$$

Where ΔP_{Solar}, and ΔP_L are the solar power, and load power variations, respectively. These variations are signs of µG disturbance signals. Whereas, the damping (D) and the inertia (H) are parameters of uncertainty.

EVs are designed as a first order lag systems [24, 36] as shown in Fig. 4, while Appendix A presents a description of the simplified random loads and photovoltaic PV.
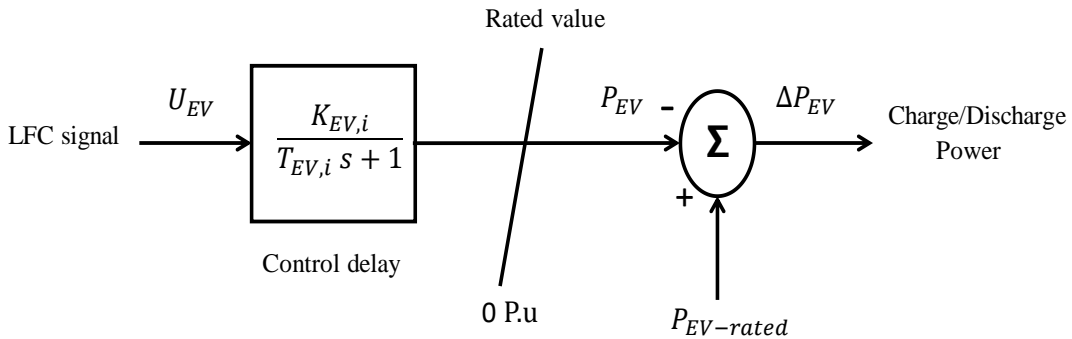

Fig. 4. EV Model.
.

5. GENERAL OVERVIEW OF HARRIS HAWKS OPTIMIZATION AND BALLOON EFFECT METHODS

5.1 Harris Hawks optimization technique

HHO is suggested by Heidari et al. [38]. This algorithm mimics the cooperative behavior of Harris' hawks to address various optimization issues. The prey is hunted by the hawks in some steps including tracing, encircling, closeness, and finally attacking. The main logic is to implement several consecutive phases to find the best (optimal) solution for a given problem. Figure 5 illustrates the main HHO phases.

A. Phase of Exploration

At this stage, the hawks perch randomly on some locations and wait to detect a prey based on the following rule:

$$X(t+1)$$
$$= \begin{cases} X_{rand}(t) - r_1|X_{rand}(t) - 2r_2X(t)| \\ \qquad\qquad\qquad\qquad\qquad if\ \alpha \geq 0.5 \\ (X_{rabbit}(t) - X_m(t)) - r_3(LB + r_4(UB - LB)) \\ \qquad\qquad\qquad\qquad\qquad if\ \alpha < 0.5 \end{cases}$$
$$(19)$$

In addition, $X_m(t)$ is the average position that determined by:

$$X_m(t) = \frac{1}{N}\sum_{i=1}^{N} X_i(t) \qquad (20)$$

Where Xi and N as the place of the hawks and their size, respectively.

B. Phase of Transition from Exploration to Exploitation

At this stage, the algorithm can transition from global to local search based on the fugitive energy of prey (E) that is modeled as:

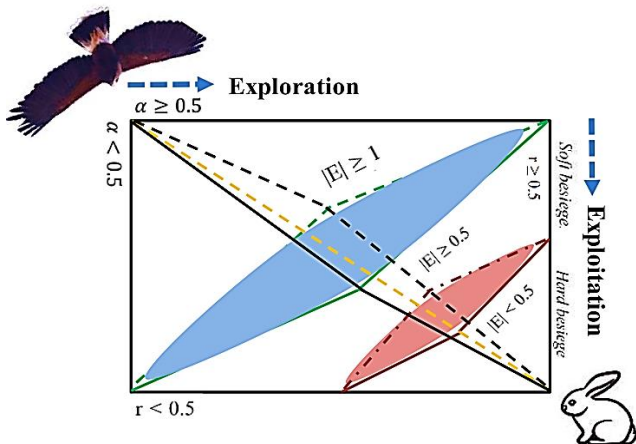$$E = 2E_0\left(1 - \frac{t}{T}\right), \quad E_0 \in [-1,1] \qquad (21)$$

Fig. 5. The main phases of the classic HHO [38].

Regarding to the value of $|E|$, it is decided to start the exploration phase ($|E| \geq 1$) or exploiting the neighborhood of the solutions ($|E| < 1$).

C. Phase of Exploitation

In this phase, the Harris' hawks perform a suddenly executed by attacking the intended prey that was discovered in the previous phase. Whatever the prey does, the hawks will cause a hard or soft besiege (trapping) to catch the prey.

In soft besiege stage, the prey (i.e. rabbit) still has enough energy at $r \geq 0.5$ and $|E| \geq 0.5$, and try to escape by some random misleading hops. This manner was updated and modeled according to the following formula:

$$X(t+1) = \Delta X(t) - E|JX_{rabbit}(t) - X(t)| \qquad (22)$$

$$\Delta X(t) = X_{rabbit}(t) - X(t) \qquad (23)$$

Where, $\Delta X(t)$ is the difference between the prey position vector and the current location in moment t, and $J = 2(1 - r)$ signifies the jump force of the prey.

In the hard besiege stage, the prey is so exhausted and has a low power for escaping when $r \geq 0.5$ and $|E| < 0.5$. Therefore, the solutions in this case are updated using the optimal solution as formulated in Eq. (24). A simple example of this step with one hawk is depicted in Fig. 6a.

$$X(t+1) = X_{rabbit}(t) - E|\Delta X(t)| \qquad (24)$$

In the soft besiege with progressive rapid dives stage, the solution has the ability to pick out their next move at ($r < 0.5$ and $|E| \geq 0.5$), and this performed using Eq. (25).

$$Y = X_{rabbit}(t) - E|JX_{rabbit}(t) - X(t)| \qquad (25)$$

To determine the rapid dives, Levi's flight is used to update the motion as:

$$Z = Y + S \times LF(D) \qquad (26)$$

In Eq. (26), $S \in R^{1xD}$ represents a vector randomly selected at 1 x D size, and LF is the levy flight that denoted as:

$$LF = 0.01 \times \frac{\mu \times \sigma}{|v|^{\frac{1}{\beta}}} \qquad (27)$$

$$\sigma = 0.01 \times \frac{\mu \times \sigma}{|v|^{\frac{1}{\beta}}}\left(\frac{\Gamma(1+\beta) \times sin(\frac{\pi\beta}{2})}{\Gamma\left(\frac{1+\beta}{2}\right) \times \beta \times 2^{\left(\frac{\beta-1}{2}\right)}}\right)^{\frac{1}{\beta}} \qquad (28)$$

The tactics that shape the hawks' position vector can be summarized in the next iteration as follows:

7

$$X(t+1) = \begin{cases} Y & \text{if } F(Y) < F(X(t)) \\ Z & \text{if } F(Z) < F(X(t)) \end{cases} \quad (29)$$

A simple illustration for one hawk is demonstrated in Fig. 6b.

At last stage called the hard besiege with progressive rapid dives, the intended prey has low energy to escape under the condition $r < 0.5$ and $|E| < 0.5$, the solutions shall be updated using the following rule:

$$Y = X_{rabbit}(t) - E|JX_{rabbit}(t) - X_m(t)| \quad (30)$$

$$Z = Y + S \times LF(D) \quad (31)$$

The position of hawks can be updated in such case as Eq. 29.

A simple example of this last step is demonstrated in Fig. 6c.

To facilitate understanding of the HHO algorithm, Table 2 presents a list of symbols used in this algorithm.

Afterwards, the designed controller for emulating the inertia response has been achieved by using the HHO. Hence, the optimal P-controller parameter is $K_p = 2.581$, which produce the optimal control signal to the virtual inertia control loop for emulating the inertia response into the μG and supporting the proposed control strategy for plug-in EVs.

Table 2 Meanings of HHO algorithm symbols.

| Description	Symbol
Hawks position vector in the next iteration.	$X(t+1)$
Prey position (best agent).	$X_{rabbit}(t)$
Current position vector of the hawks.	$X(t)$
Random numbers within [0, 1].	$r_1, r_2, r_3, r_4, \alpha$
Lower, upper bounds of the variables, and dimension.	LB, UB, D
One existing hawks that selected randomly.	$X_{rand}(t)$
Hawks average position	$X_m(t)$
Swarm size, iteration counter, Max. iterations	N, t, T
Fugitive energy of prey, initial state of energy	E, E_0
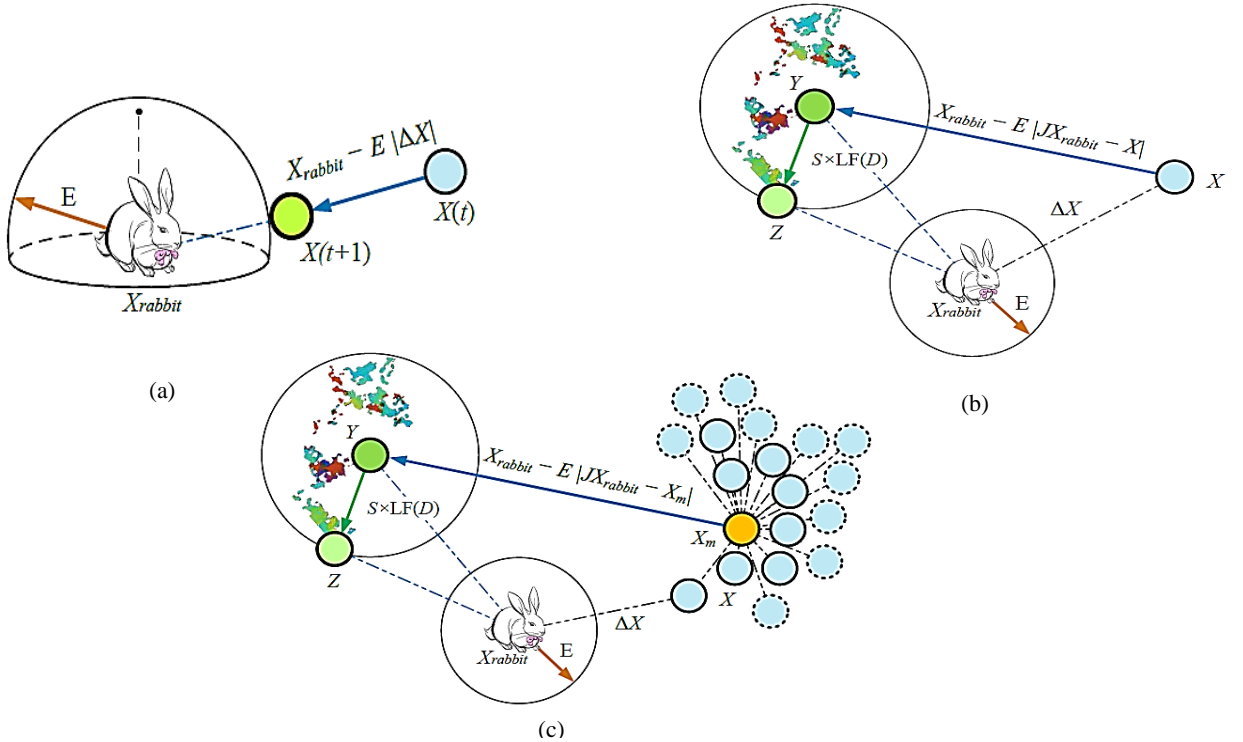
Fig. 6. Example of overall vectors in the case of: a) Hard besiege, b) Soft besiege with progressive rapid dives.
c) Hard besiege with progressive rapid dives in 2D space.

5.1 Idea of Balloon Effect and Its Principle Operation

BE is firstly proposed for electrical systems applications in [39-41] for tuning the PID controller gains for LFC and the position of armature-controlled DC motor. At any iteration, the objective function depends only on the value of the controller' gains [47]. This means that there is no direct effect of system changes on the objective function, and this leads to weak reaction of the optimizer in case of the issues that happened within the system. For the mentioned reasons, BE was designed to treat this point. The idea of BE is illustrated in Fig. 7.
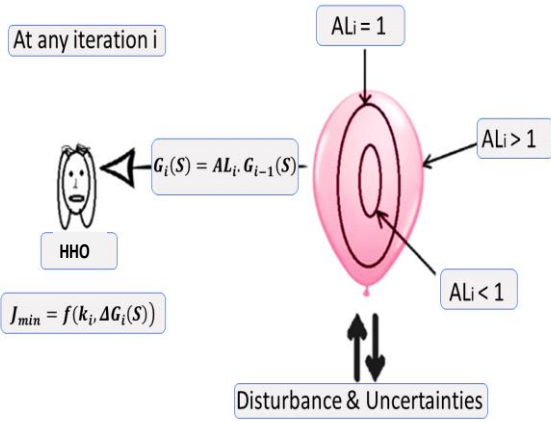
Fig. 7. The main Concept of Balloon Effect at any iteration (i).

BE has been applied to increase the interactivity of HHO with the on-line system issues such as system disturbances and parameter variations, and enhance the algorithm process. The expression 'BE" represents the effect of the system changes on the system's open loop transfer function, which is similar to the effect of the air on the size of balloon.

As shown in Fig. 7, for any iteration (i), the plant of open loop transfer function $G_i(S)$ can be determined by:

$$G_i = \frac{Y_i(s)}{U_i(s)} \qquad (32)$$

Additionally, $G_i(S)$ can be computed using its nominal value of the plant $G_0(S)$ as:
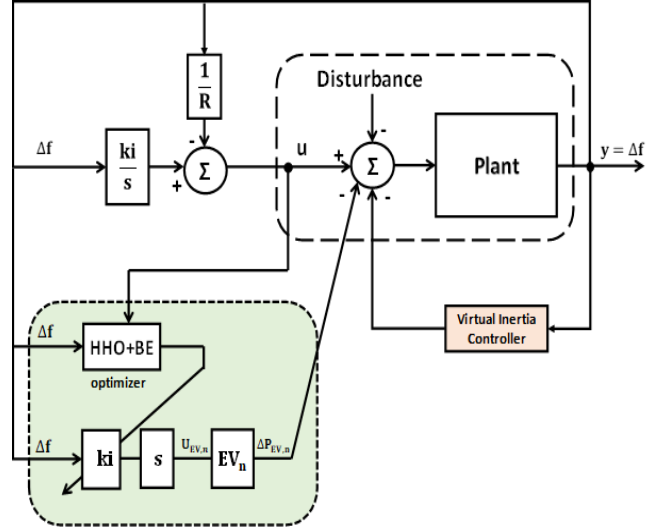
$$G_i = AL_i . G_{i-1}(S) \qquad (33)$$

where, AL_i is a parameter coefficient such that:

$$G_{i-1}(S) = \rho_i . G_0(S) \qquad (34)$$

$$\text{where,} \qquad \rho_i = \prod_{n=1}^{i-1} AL_n \qquad (35)$$

The simplified block diagram of the proposed system with modified HHO based BE supported by virtual inertia controller for adaptive EVs integral control system is shown in Fig. 8. It can be noted that: at any iteration i, main output

n=1, 2, 3, 4, 5.

Fig. 8. Simplified microgrid model based adaptive control system supported by BE for EVs with helps of virtual inertia controller.

$Y_i(s)$ and input $U_i(s)$ will be fed to the optimizer to calculate the actual process transfer function at this moment i and it used only to stop calculation if it lies within a small deviation (about 0.001 pu).

6 ROBUSTNESS AND STABILITY OF PROPOSED HHO BASED BE SCHEME

Figure 9 presents the block diagram of the proposed control system, and it can be expressed as [48]:

$$\left. \begin{array}{l} \dot{X}_p = A_p X_p + b_p c_0^* r \\ y_p = C_p^T X_p \end{array} \right\} \qquad (36)$$

Considering the nominal plant $G_0(S)$ as the base of the proposed adaptive controller, in the case of nominal parameters, the system output will be defined as:

$$y^* = G_0(S). u \qquad (37)$$

Now, the actual output:

$$y(t) = y^* + H_a . u(t) \qquad (38)$$

$$H_a = G_i(S) - G_0(S) \qquad (39)$$

It is assumed that H_a is a casual operator satisfying

$$\|H_a . u(t)\|_\infty \le \gamma_a \|u(t)\|_\infty + \beta_a \qquad (40)$$

Where γ_a and β_a are two constants with small values, and for all t ≥ 0, β_a may include the possible presence of output bounded disturbance.

9

The theorem that ensures a guarantee for the stability of the adaptive system in the presence of parameter uncertainties has proven in [48] which it is assumed that the trajectories of the adaptive system are continuous with respect to time (t).
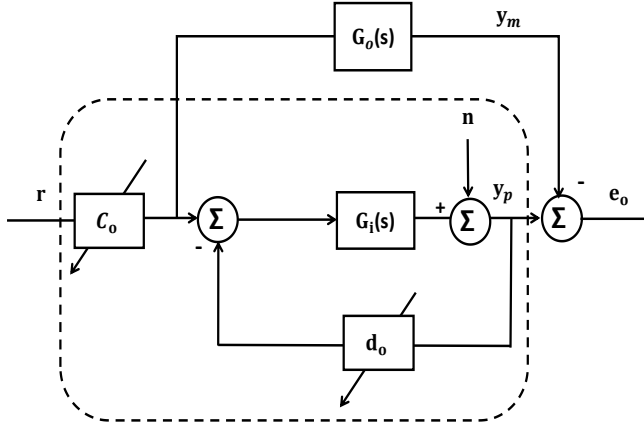

Fig. 9. System' block diagram for stability [48].

7. CONTROL STRATEGY AND PROBLEM FORMULATION

7.1 Adaptive integral controller design based on HHO algorithm.

The PID and P controllers cannot yield sufficient control performance with the consideration of nonlinearities and parameter variations [26, 36]. To overcome these problems, the integral I- controller has been used for system control. In this manner, the suggested coordinated control strategy relies on the integral controller considering RESs penetration [37]. It has validated to be remarkably effective in the regulating of a wide range of processes. However, the I-controller suffers from a complicated process of parameters tuning-based trial and error method. Considering the advantages of HHO algorithm and BE that mentioned before, this paper uses HHO algorithm based BE to find the optimum gain value of the integral controller for plug-in EVs to reduce the deviations in system frequency besides balancing the power generation and demand load power.

In this work, the integral squared-error (ISE) has been selected as the main objective function (Obj) to tune the controller parameters. This objective accounts for maintaining the frequency and power exchange at its predefined values as soon as possible under any kind of load change or system disturbances. It can be formulated as follows:

$$Obj = min \sum_{i}^{N} Ki_{,i} \left\{ \int_{0}^{t_{sim}} ((\Delta f)^2 + (\Delta P_d)^2)) \, dt \right\}$$
$$+ max \sum_{i}^{N} Ki_{,i} \int_{0}^{t_{sim}} (\Delta P_{EV,i})^2 \, dt \quad (41)$$

Subject to constraints of the integral I-controller gain parameter as

$$K_i^{min} \leq K_i \leq K_i^{max} \quad (42)$$

7.2 Frequency regulation based on HHO supported by BE for plug-in electric vehicles design

The imbalance between the demand of real power and its generation at an agreeable nominal frequency causes a problem in LFC. Therefore, modified HHO based BE was introduced to know its effectiveness in resolving these issues within LFC. The suggested initial parameters of the classic HHO optimizer was listed in Table 3.

7.2.1 HHO without Balloon Effect

Figure 10 describes a general power system block diagram with prospective classic HHO technique for any area (n), where EV$_n$ output is considered as input to the μG.

The purpose of system planning model is to minimize the overall cost in power generated ΔP_M. For this reason, by considering ($\Delta P_{Load}'' = 0$), it is better to convert the system into closed loop second order one for getting an objective function (Obj) as in Eq. (37) with standard parameters for the controlled load. Therefore, we can calculate ISE as a function in $\{M_p, T_r, T_s\}$ that calculated by finding ω_n and η parameters as:

$$T.F = \frac{\omega_n^2}{S^2 + 2\eta\omega_n S + \omega_n^2} =$$
$$= \frac{\frac{k_i}{M_o}}{S^2 + \left(\frac{(D_o + 1)}{M_o}\right) S + \frac{k_i}{M_o}} \quad (43)$$

$$\omega_n = \sqrt{k_i/M_o}, \quad and \quad \eta = \frac{1}{2T_{EV} \cdot \sqrt{k_i/T_{EV}}}$$
$$= \frac{\left(\frac{(D_o + 1)}{M_o}\right)}{2 \cdot \omega_n} \quad (44)$$

$$T_r = \left(\frac{\pi - \sqrt{(1 - \left(2T_{EV} \cdot \left(k_i/T_{EV}\right)^{0.5}\right)^2}}{\left(k_i/T_{EV}\right)^{0.5} \cdot \sqrt{\left(1 - \left(2T_{EV} \cdot \left(k_i/T_{EV}\right)^{0.5}\right)^2}} \right)$$
$$= \frac{\pi - \left(1 - \left(\frac{\left(\frac{(D_o + 1)}{M_o}\right)}{2 \cdot \omega_n}\right)^2\right)^{0.5}}{\omega_n \cdot \left(1 - \left(\frac{\left(\frac{(D_o + 1)}{M_o}\right)}{2 \cdot \omega_n}\right)^2\right)^{0.5}} \quad (45)$$

10

$$M_P = e^{\dfrac{(-\pi/T_{EV})}{2\left(k_i/T_{EV}\right)^{0.5}\sqrt{\left(1-\left(\left(2T_{EV}\cdot\left(k_i/T_{EV}\right)^{0.5}\right)\right)^2\right)}}}$$

$$= e^{\left(\dfrac{-\pi\,(D_o+1)}{2M_o\omega_{n^*}\sqrt{\left(1-\left(\dfrac{((D_o+1))}{2.\,M_o\omega_n}\right)^2\right)}}\right)} \tag{46}$$

$$T_s = \left(\dfrac{4}{\left(k_i/T_{EV}\right)^{0.5}\cdot\dfrac{1}{2T_{EV}\cdot\sqrt{k_i/T_{EV}}}}\right) = \dfrac{8}{\left(\dfrac{(D_o+1)}{M_o}\right)} \tag{47}$$

The dynamic relationship of generator-load between the supply error (ΔP_M-$\Delta P''_L$) and frequency deviation Δf is expressed as follows:

$$\dot{\Delta f} = \left(\frac{1}{2H}\right)(\Delta P_M - \Delta P''_{Load}) - \left(\frac{D}{2H}\right).\Delta f \tag{48}$$

$$\dot{\Delta f} = \left(\begin{array}{c}\Delta P_L + \Delta P_{Inertia} - \Delta P_{PV} + \Delta P_{EV} \\ (Participation\ of\ the\ remnant\ EVs\ units)\end{array}\right) \tag{49}$$

Table 3 Suggested initial HHO Parameters:

Parameter	Value
No. of iterations (t)	50
No. of design variables	1
No. of search agents	5
Initial (Ki) controller	[0.10, 0.12, 0.25, 0.33, 0.40]
Lower Bound (LB)	-5
Upper Bound (UB)	+5

7.2.2 HHO with Balloon Effect

According to the simplified model of the proposed μG with HHO+BE shown in Fig. 11. It can be noted that at any iteration i,

$$G_i(S) = AL_i.\rho_i.G_o(S) \tag{50}$$

where,
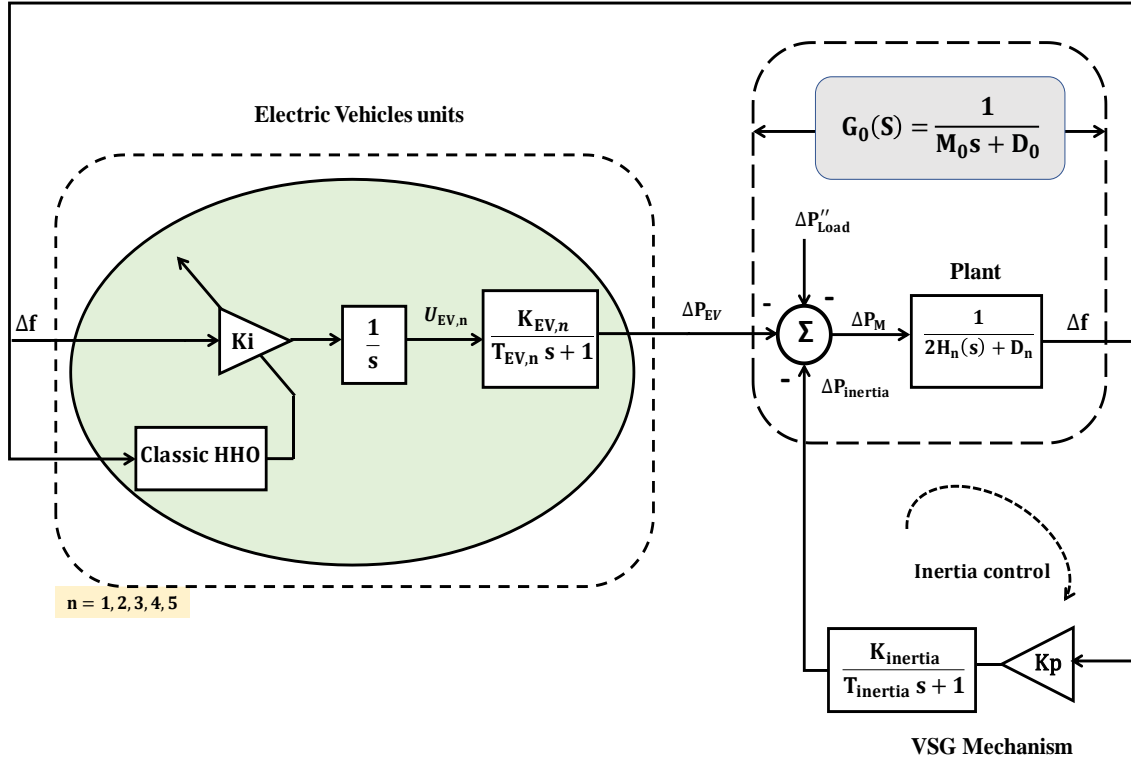
$$G_o(S) = \frac{1}{M_o S + D_o} \tag{51}$$

Fig. 10. Blok diagram of reduced area with controlled EVs only based on classic HHO supported by virtual inertia for any controlled loads (n).
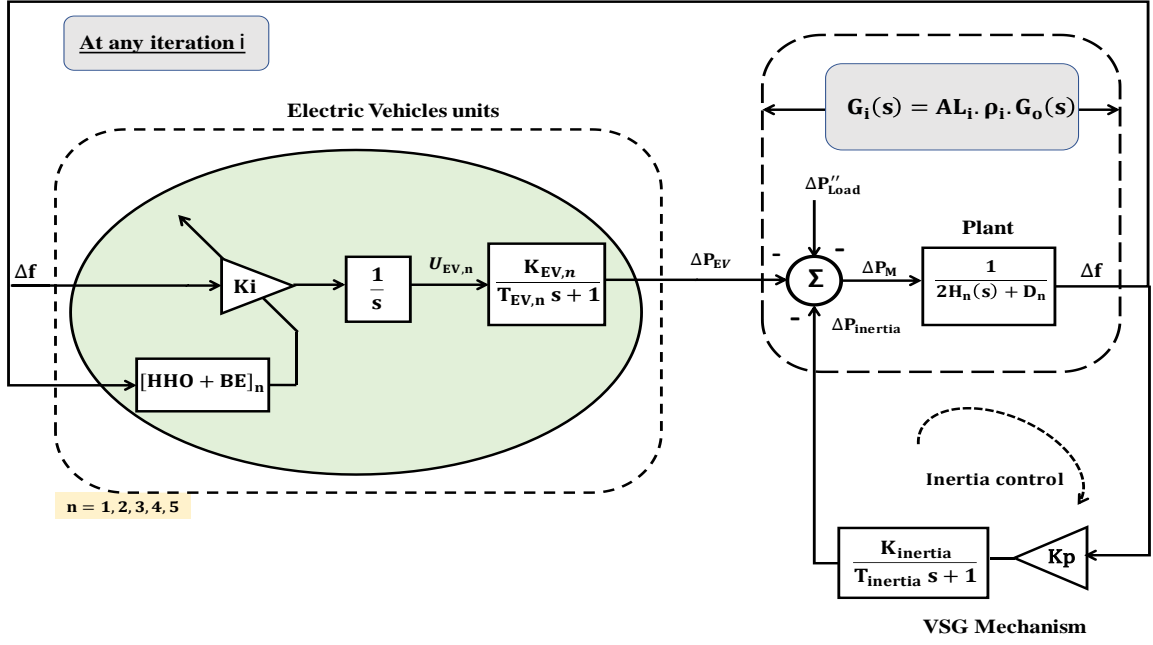
Fig. 11. Reduced microgrid model controlled based BE for EVs control system in presence of virtual inertia.

Therefore, the closed loop transfer function at any iteration (i) can be calculated as:

$$T.F = \cfrac{\left(\cfrac{k_i . AL_i . \rho_i}{M_o}\right)}{S^2 + \left(\cfrac{(D_o + AL_i . \rho_i)}{M_o}\right)S + \left(\cfrac{k_i . AL_i . \rho_i}{M_o}\right)} \quad (52)$$

Then

$$\omega_n = \sqrt{\left(\cfrac{k_i . AL_i . \rho_i}{M_o}\right)}, and \quad \eta = \cfrac{\left(\cfrac{(D_o + AL_i . \rho_i)}{M_o}\right)}{2 . \omega_n} \quad (53)$$

$$M_P = e^{\left(\cfrac{-\pi (D_o + . AL_i . \rho_i)}{2M_o\omega_n * \sqrt{\left(1 - \left(\cfrac{((D_o + . AL_i . \rho_i))}{2 . M_o \omega_n}\right)^2\right)}}\right)} \quad (54)$$

$$T_r = \cfrac{\pi - \left(1 - \left(\cfrac{\left(\cfrac{(D_o + . AL_i . \rho_i)}{M_o}\right)}{2 . \omega_n}\right)^2\right)^{0.5}}{\omega_n . \left(1 - \left(\cfrac{\left(\cfrac{(D_o + . AL_i . \rho_i)}{M_o}\right)}{2 . \omega_n}\right)^2\right)^{0.5}} \quad (55)$$

$$T_s = \cfrac{8}{\left(\cfrac{(D_o + . AL_i . \rho_i)}{M_o}\right)} \quad (56)$$

It is clear now that the objective function at any iteration (i) is a function in k_i, AL_i ($Obj = f(k_i , AL_i)$). This means that any change in the system parameters or the load demand will appear immediately as a change in the value AL_i, which leads to a change in the objective function at this iteration and will increase the ability of HHO to address the system difficulties.

Using a "certainty equivalence controller" [49], the control input can be described as:

$$U(s) = \left(\cfrac{k_i}{S + \breve{G}k_i}\right) R(s) \quad (57)$$

With considering a discrete time domain, it can be noted that:

$$U(k) = f\left(\breve{G}(k), R(k + d)\right) \quad (58)$$

Where $d \geq 1$ is the delay between the input and output. The effects of nonlinearity, load disturbance and uncertainty in the parameters are instantaneously included in the determined open loop transfer function $G_i(S)$ or $\breve{G}$ detailed in Fig. 12.
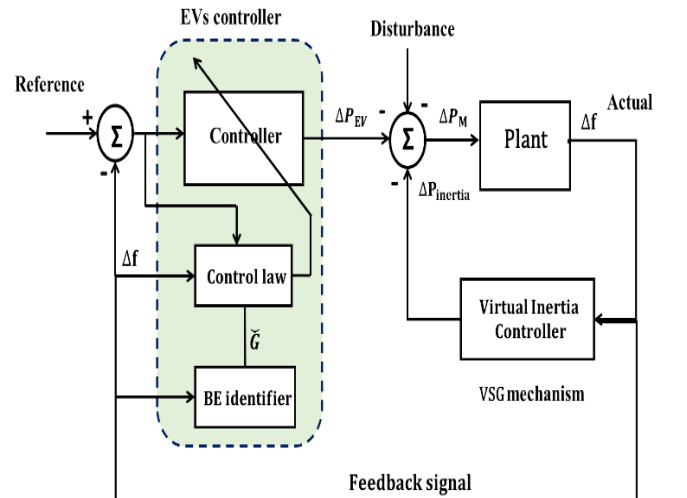

Fig. 12. Adaptive control model using balloon effect identifier.

12

The stability of the system with the proposed control scheme can be tested using the reduced system model by adding a filter to reduce the effect of output noise as shown in Fig. 13.
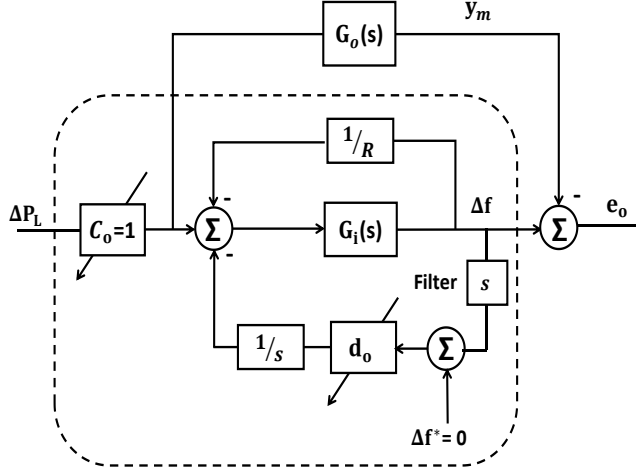

Fig. 13. Reduced MG model for testing the stability.

Assuming $c_0 = 1$ and at any iteration i, the effect of system parameter changes can appear in $G_i(S)$ value, as in Eq. (52), the transfer function between the output frequency deviation to the load power change ΔP_L can be represented as:

$$\frac{\Delta f}{\Delta P_L} = \frac{G_i(S)}{1 - d_0 G_i(S)} = \frac{AL_i.\rho_i}{MS + (D_o + AL_i.\rho_i) - d_0.AL_i.\rho_i} \quad (59)$$

Therefore, to maintain system stability, the following condition should be satisfied.

$$d_0 \leq \left(\frac{D_o}{AL_i.\rho_i} + 1\right), \text{where } d_0 = k_i$$

8. PERFORMANCE ASSESSMENT OF HHO BASED BALLOON EFFECT

In this section, a statistical results analysis for different benchmark test functions are presented in Table 4. These functions can be used to analyze the exploitation ability of the optimization algorithm, since there is only one global optimal solution and no other local optimal solution exists.

A comparative performance analysis of modified HHO based BE with PSO, Jaya, and classic HHO was described in Table 5. The same number of populations and iterations have been used in each test function for resolving the optimization issues. A total of 20 independent running processes are performed for all algorithms, the best and worst values of these functions are noted by taking 50 population size and 50 number of iterations. The proposed approach gives superior to the other algorithms in terms of the best and worst

In general, the validation of the optimization algorithm depends on its speed convergence with optimum value. The optimal value of Obj. for 50 population size is plotted against the number of J-evaluation in Fig. 14. It noted that the proposed method converges relatively faster than other meta-heuristics techniques.

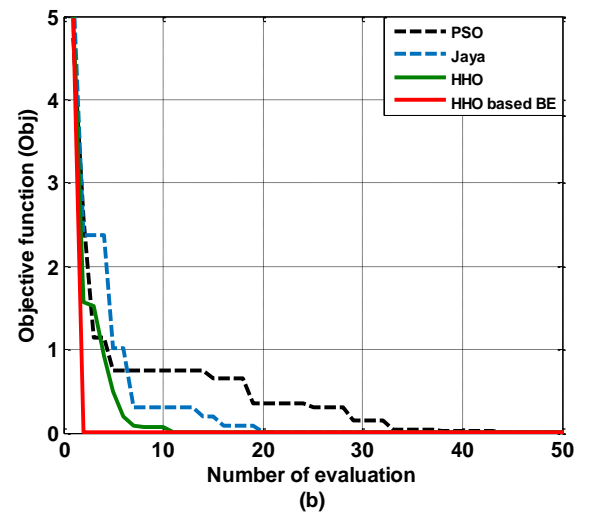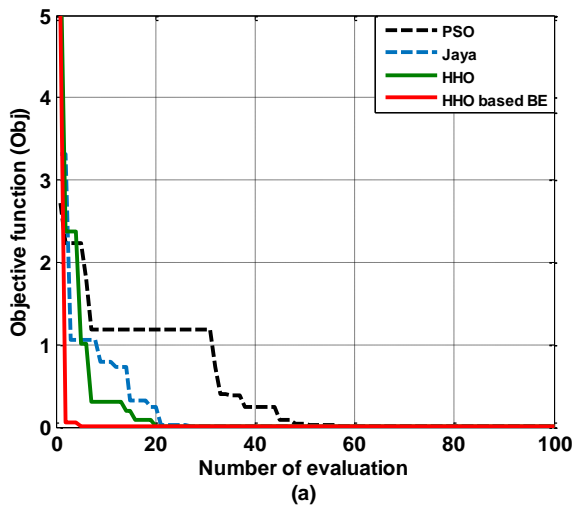Finally, Fig. 15 shows the overall flowchart that included all previous procedures.

Fig. 14. Speed convergence characteristics of classic PSO, Jaya, HHO, and modified HHO based BE for:
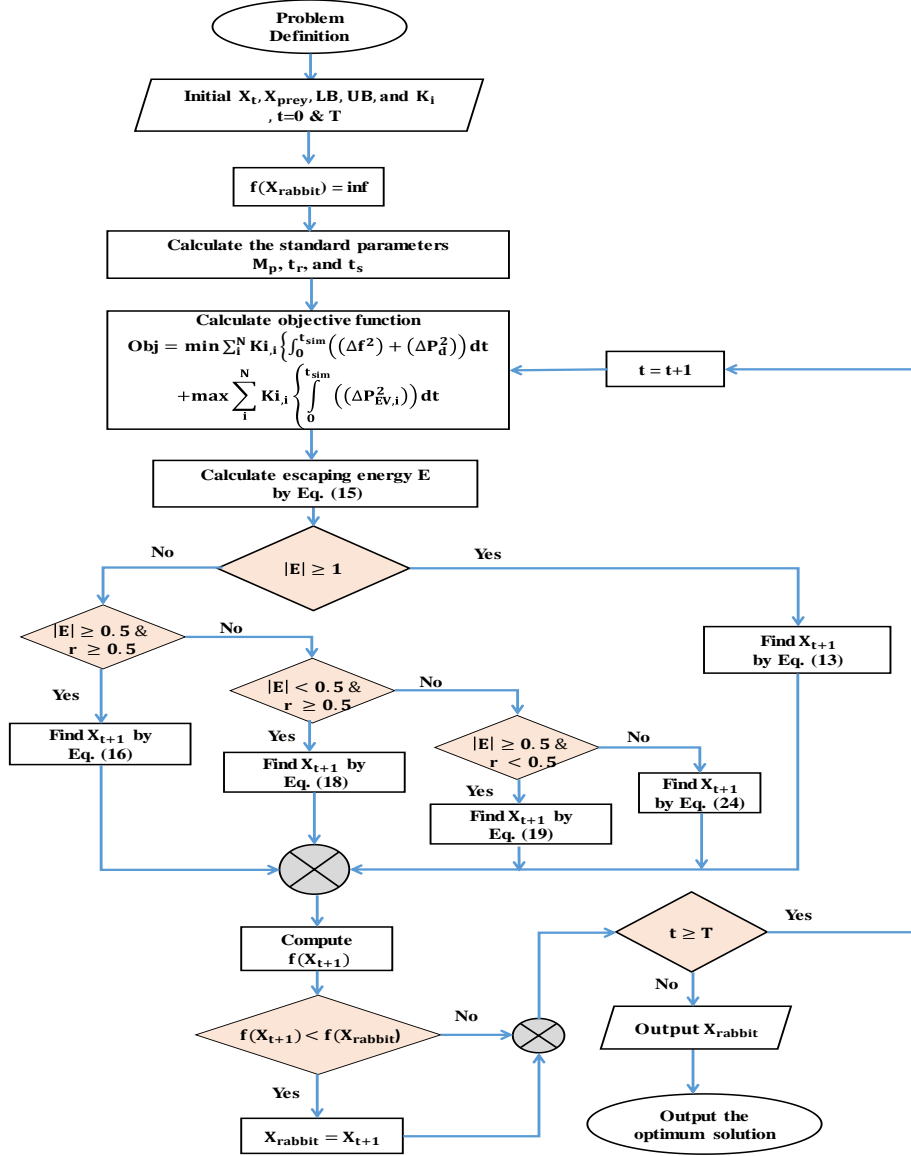a) Matyas test function   b) Rastrigin test function

Fig. 15. Overall flowchart of the main procedures of Harris Hawks with the proposed control strategy.

Table 4 Description of benchmark test functions.

Function name	Formula	D	Search domain	f_{min}
Sphere	$f(x) = \sum_{i=1}^{d}(x_i^2)$	d	$[-\infty, \infty]$	0
Matyas	$f(x) = 0.26(x_1^2 + x_2^2) - 0.48x_1x_2$	2	[-100,100]	0
Schaffer N. 2	$f(x) = 0.5 + \dfrac{sin^2(x_1^2 - x_2^2) - 0.5}{[1 + 0.001(x_1^2 + x_2^2)]^2}$	2	[-100,100]	0
Rastrigin	$f(x) = -10d + \sum_{i=1}^{d}(x_i^2 - 10\cos(2\pi x_i)$	d	[-5.12,5.12]	0
Ackley	$f(x) = -20\exp\left(-0.2\sqrt{\dfrac{1}{d}\sum_{i=1}^{d}x_i^2}\right) - exp\left(\dfrac{1}{d}\sum_{i=1}^{d}\cos(2\pi x_i)\right) + 20 + \exp(1)$	d	[-5,5]	0

14

Table 5 Comparative performance indexes of different test functions,

Functions	D^a	Search space	Statistical values	PSO	Jaya	HHO	HHO+BE
Sphere	5	[-5,5]	Best	$1.79e^{-08}$	$4.77e^{-14}$	$1.78e^{-19}$	$5.16e^{-31}$
			Worst	$1.82e^{-08}$	$4.77e^{-14}$	$1.82e^{-18}$	$5.22e^{-30}$
Ackley	5	[-5,5]	Best	$3.85e^{-05}$	$2.70e^{-16}$	$1.56e^{-27}$	$0.00e^{+0}$
			Worst	$3.88e^{-05}$	$2.70e^{-16}$	$1.48e^{-26}$	$0.00e^{+0}$
Matyas	5	[-5,5]	Best	$1.52e^{-11}$	$4.22e^{-11}$	$2.36e^{-15}$	$2.71e^{-27}$
			Worst	$1.63e^{-11}$	$4.26e^{-11}$	$2.42e^{-15}$	$2.74e^{-27}$
Schaffer N.2	5	[-5,5]	Best	$0.00e^{+0}$	$0.00e^{+0}$	$0.00e^{+0}$	$0.00e^{+0}$
			Worst	$0.00e^{+0}$	$0.00e^{+0}$	$0.00e^{+0}$	$0.00e^{+0}$
Rastrigin	5	[-5,5]	Best	$2.11e^{-09}$	$3.09e^{-09}$	$9.29e^{-18}$	$0.00e^{+0}$
			Worst	$1.94e^{-09}$	$3.22e^{-09}$	$9.33e^{-18}$	$0.00e^{+0}$

9. RESULTS AND DISCUSSIONS

In this study, a coordination of control strategy between the inertia control, i.e., auxiliary LFC, and the control of secondary frequency loop with integration of EVs is suggested to improve the islanded μG frequency stability in case of high penetrations resulted by RESs and random loads. Where, the proposed coordinated control strategy relies on I-controller, which is optimally designed by the HHO based BE to obtain the minimum value of the frequency deviations for proposed system. Moreover, the performance of the suggested coordinated control strategy is compared with system using CDM as in [17] with/without virtual inertia controller under high RESs penetrations and integrations of EVs.

Simulation results for the studied μG are implemented using the professional software MATLAB/Simulink to validate the efficacy of the coordinated proposed control strategy. The HHO code is linked as an m-file to the model for optimization process. Frequency stability is examined with the proposed strategy under different operating conditions through the following scenarios:

Note; the colors that used in the following graphs as: Black indicates to CDM without virtual inertia, blue indicates to CDM + virtual inertia, green indicates to classic HHO + virtual inertia, and red indicates to HHO based BE + virtual inertia.

Scenario A: Performance evaluation of the μG with nominal system parameters

In this section, the performance of the islanded μG with the proposed adaptive control strategy (HHO based BE) for plug-in electric vehicles EVs supported by virtual inertia control and compared to another robust CDM controller is demonstrated in Table 6, and investigated using the nominal system parameters as given in Table 1. This studied case is divided into two scenarios that performed with/without the effect of RESs uncertainties and random loads.

Scenario A.1: Without the effect of RESs uncertainties and random loads.

In this scenario, the studied μG performance with the proposed control strategy is tested and assessed by subjecting different load patterns into five stages. First, 10% of the load is added at 25 sec, and then followed by 10% of the load at 50 sec. After that, the load is shed at 75 sec by 25% and followed by a further 5% of the load connected at 100 sec as shown in Fig. 16.

Figure 17 illustrates the efforts of HHO based BE and classic HHO, it can be noted that BE exerted more efforts to improve the overall system response.

Figure 18 displays the system response of the studied μG with different control strategies in case of the EVs control system based CDM controller in presence /absent of virtual inertia, modified HHO based BE supported by virtual inertia controller under the impact of the previous load variations.

Figure 18(a) shows the frequency deviations of the μG in case of load injection and shedding operation conditions of 10%, 10%, 25% and 5% of load variations at 25 s, 50 s, 75 s and 100 s respectively for PEVs as shown in Fig.16 by using the proposed control strategy (HHO based BE supported by virtual inertia) and compared with the classic HHO, and CDM without/with virtual inertia that described in Table 6.

Thus, it is clear that the proposed control strategy with HHO based BE in presence of virtual inertia control gives superior performance and more reduction of the frequency excursions compared to other ones against the case of disturbance change. In addition, it can deal efficiently with these issues and offers more robustness and better performance with the smallest oscillation, a lower steady-state error and settling time.
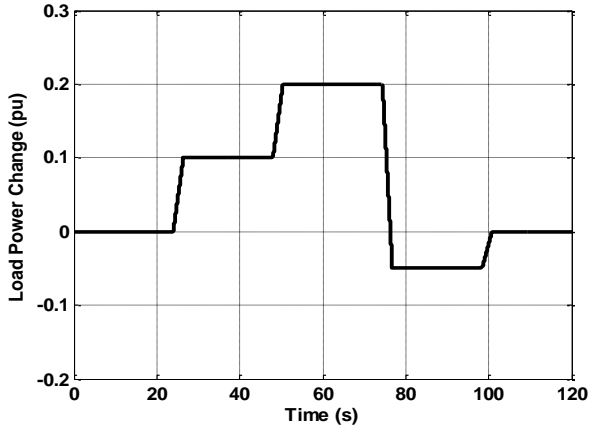
Fig. 16. Variable load power change.

(a) System Frequency deviation

Figure 18(b) describes that the needed diesel power ΔP_d produced by the proposed control strategy has best time response comparing with those of other controllers in presence of electric vehicles in (discharging mode). Figure 18(c) indicates that how large the discharging occurred in the power of PEVs by proposed control strategy scheme at the moment of the disturbance for a system with controller tuned by adaptive HHO based BE. It is clarified from Fig 18c. and Table 6 that the discharged power of PEVs in case of the suggested controller is higher than those of the other ones due to the larger amount of power participation into μG in less time period at the disturbance moment and return more fast than other controllers to steady state with less power due to the presence of the virtual inertia. In addition, the proposed control scheme using HHO can avoid the problem of steady state error that appeared with CDM controller.

Figure 19 illustrates the interaction between the power change of the virtual inertia $\Delta P_{inertia}$ for CDM, classic HHO, and modified HHO based BE. It is noted from Fig. 19 and Table 6 that the system with adaptive HHO based BE can decrease the total variations in the power of the virtual inertia as compared to CDM controller and standard HHO.
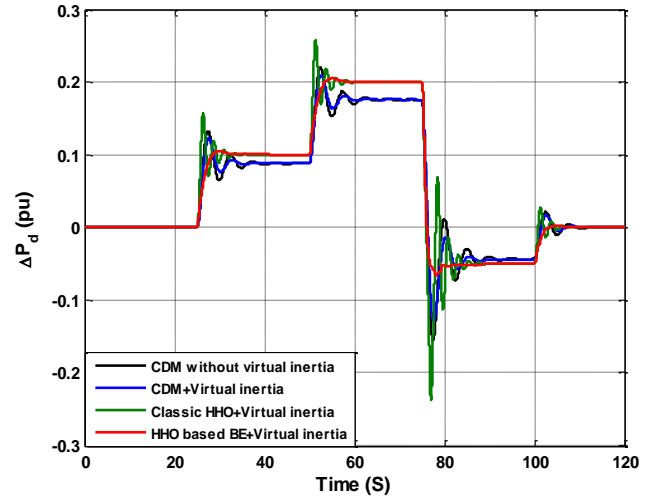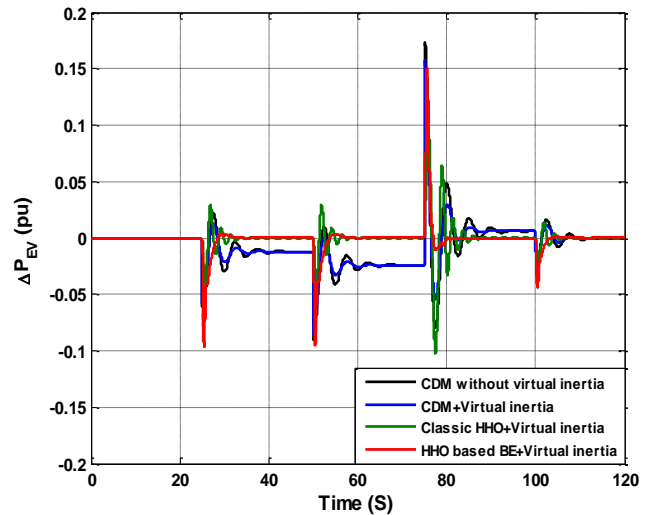

(b) Power change in diesel generator.

**Fig. 17.** Ki output control signal for HHO with /without BE.

(c) PEVs discharging power.

Fig. 18. System response for Scenario A.1

16

Table 6 Measurements of the proposed control strategies related to scenario A. 1.

Parameter	Index	CDM without virtual inertia	CDM + virtual inertia	Classic HHO + virtual inertia	HHO based BE + virtual inertia
Δf	Min.	-0.07724	-0.05371	-0.1377	-0.04972
	Max.	0.15180	0.13330	0.16110	0.17560
	Mean	$2.23e^{-06}$	$-3.78e^{-06}$	$-2.22e^{-06}$	$-4.75e^{-06}$
	STD	0.02067	0.01719	0.02017	0.01153
ΔP_d	Min.	-0.15530	-0.12930	-0.02374	-0.06569
	Max.	0.22050	0.21010	0.25690	0.20511
	Mean	0.04578	0.04578	0.05208	0.05104
	STD	0.08225	0.08160	0.09359	0.09001
ΔP_{EV}	Min.	-0.09093	-0.08471	-0.10250	-0.09580
	Max.	0.17250	0.15720	0.10620	0.15090
	Mean	-0.00630	-0.00630	$1.24 e^{-06}$	-0.00109
	STD	0.02166	0.01853	0.01423	0.01469
$\Delta P_{inertia}$	Min.		-0.01532	-0.05791	-0.01697
	Max.	No virtual inertia is used in this case	0.03209	0.06391	0.05847
	Mean		$-2.40e^{-06}$	$2.03 e^{-06}$	$5.35e^{-05}$
	STD		0.00424	0.00817	0.00412
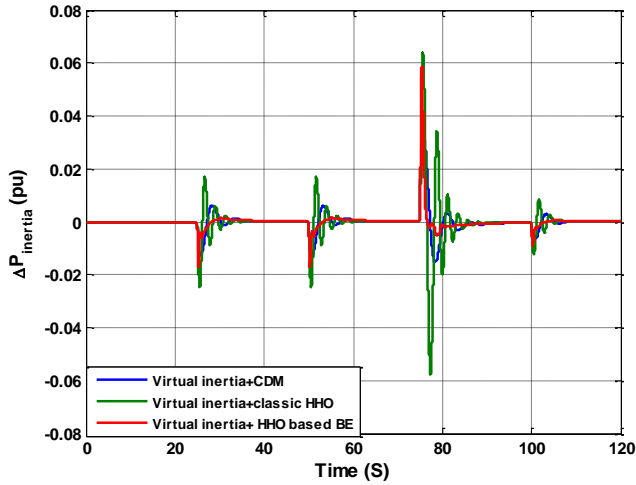
Fig. 19. Power variation of VSG for scenario A.1

Scenario A.2: With the effect of the RESs uncertainties and random loads.

In this scenario, the system has been examined to evaluate the performance of the studied μG with the proposed control strategy under the effect of the RESs uncertainties (fluctuations resulted from the PV source) and random loads connection with the same nominal parameters as mentioned in scenario A (nominal case) beside using EVs in charging mode (act as loads). Therefore, the studied μG system is tested into two subcases:

Case1: Full time injection of the RESs uncertainties and Random loads.

Figure 20 shows the variation patterns of random load and solar power. Figure 21(a) indicates that the deviation of frequency with suggested adaptive control strategy with HHO based BE is approximately equals to $\pm$ 0.0007 Hz, while this deviation arrives to $\pm$ 0.0019 Hz in case of classic HHO in presence of virtual inertia, for CDM controller, the deviation arrives to $\pm$ 0.0023 Hz in presence of virtual inertia, and approximately equals to $\pm$ 0.0031 Hz without virtual inertia controller. These results support the frequency enhancement using the proposed adaptive control strategy.
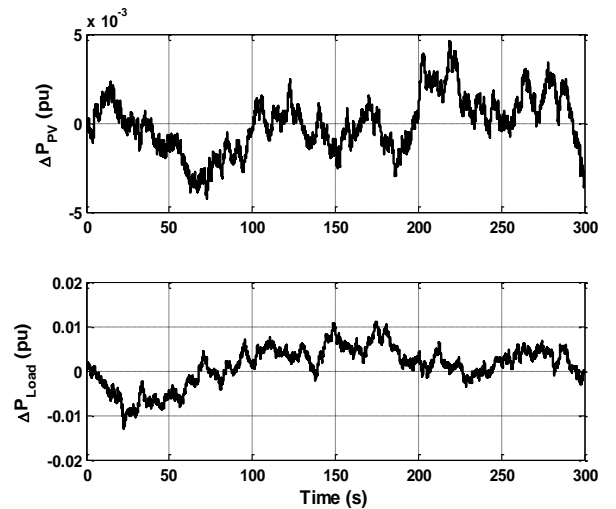

Fig. 20. Solar power and random load.

Figure 21(b) indicates that the diesel power ΔP_d in case of adaptive HHO based BE for EVs supported by virtual inertia controller is changed around ± 0.0014 pu, while this arrives to ± 0.0048 pu in case of classic HHO. For CDM controller, it approximately equals to ± 0.0083 pu in presence of virtual inertia, and approximately equals to ± 0.0095 pu without virtual inertia controller. Therefore, the required ΔP_d for proposed adaptive control strategy is smaller than that those of classic HHO, and CDM controller with/without virtual inertia controller under the effect of the fluctuations resulted from solar PV source and random loads.

(a) Frequency deviation response.

(b) Power change in diesel generator.
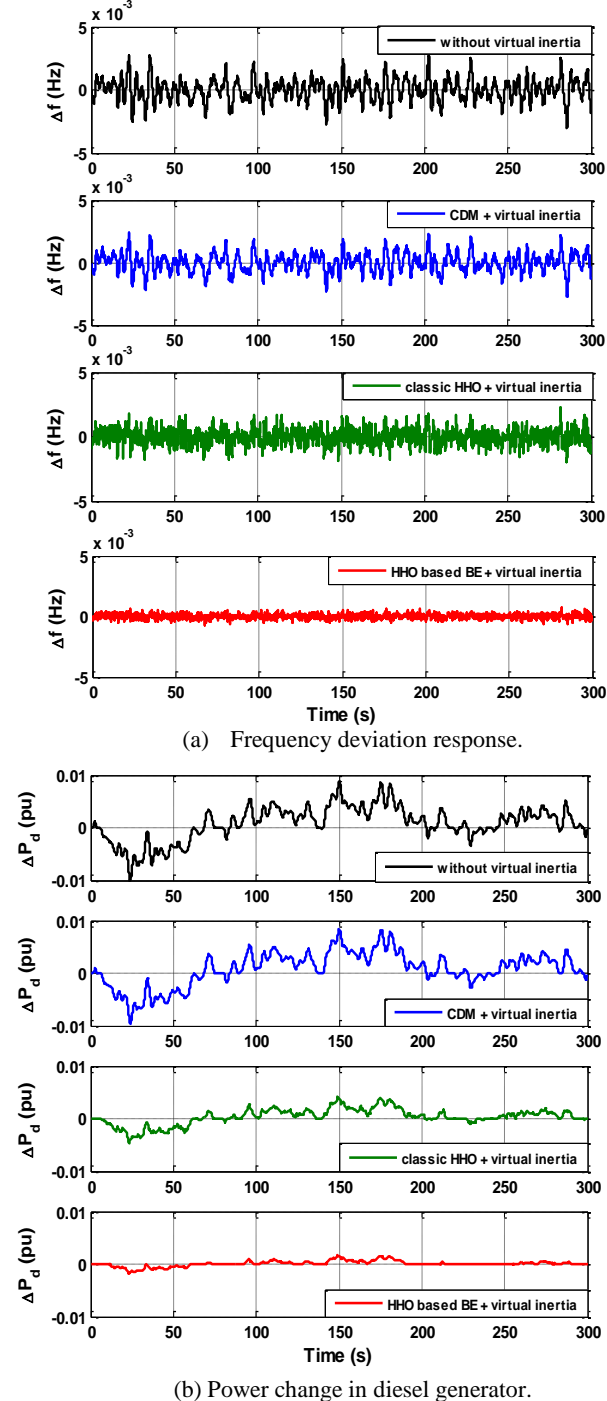
Fig. 21. System response for case 1 for scenario A.2.

Case2: Partial time injection of the RESs uncertainties and Random loads.

By connecting PV power source from 50 sec to 300 sec. additionally, the random load power is connected at multiple operation time: plug in at 125 sec and plug out at 220 sec.

Figure 22 indicates that the system response in case of the amount of discharging/charging power from electric vehicles, diesel power consumption (power losses) and the deviation in frequency with the proposed adaptive control strategy using HHO based BE beside supported by virtual inertia controller is less than the deviations in case of classic HHO algorithm and CDM with/without virtual inertia at the suggested partial disturbance injection of (PV + random loads). These results are supported by numerical evidence as shown in Table 7. Form Fig. 22 and Table 7, the frequency and power enhancement using the proposed adaptive control strategy have the superiority as compared with the classic HHO and CDM controller in presence of virtual inertia controller.

Figure 23 illustrates the power change of the virtual inertia in presence of modified HHO based BE, classic HHO, and CDM controllers. It is clear from Fig. 23 and Table 7 that the system with HHO based BE can decrease the overall variation in the power of the virtual inertia as compared to the other ones.

Finally, simulation results from case 1 and case 2 show that the transient performance has been significantly enhanced in steady state error and over/undershoot for the proposed adaptive control strategy using HHO based BE for EVs control loop under the impact of RESs uncertainties and random loads in presence of virtual inertia.
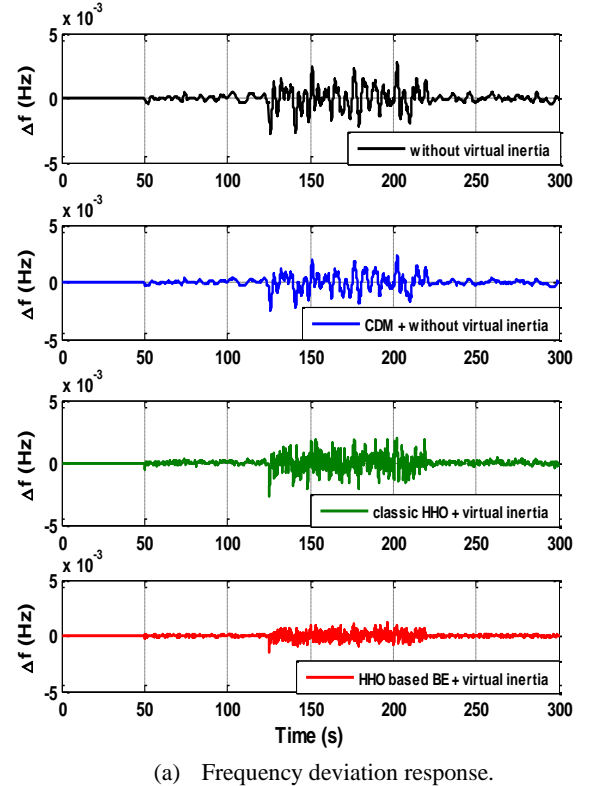

(a) Frequency deviation response.

18

Table 7 Measurements of the adaptive controllers in case of Partial time injection of the RESs uncertainties and Random loads related to case 2 in scenario A.

Parameter	Index	CDM without virtual inertia	CDM + virtual inertia	Classic HHO + virtual inertia	HHO based BE + virtual inertia
Δf	Min.	-0.002784	-0.002457	-0.002682	-0.001455
	Max.	0.002742	0.002329	0.001959	0.001154
	Mean	-3.564e^{-06}	-3.854e^{-06}	-2.426e^{-06}	-7.872e^{-07}
	STD	0.000570	0.000484	0.000406	0.000193
ΔP_d	Min.	-0.001963	-0.001360	-0.000263	0
	Max.	0.008775	0.008464	0.004696	0.001975
	Mean	0.000986	0.000987	0.000523	0.000166
	STD	0.001974	0.001960	0.001061	0.000401
ΔP_{EV}	Min.	-0.003327	-0.002943	-0.005405	-0.00850
	Max.	0.001945	0.001691	0.001714	0.002218
	Mean	-0.000164	-0.000163	-0.000627	-0.001083
	STD	0.000608	0.000526	0.00124	0.002075
$\Delta P_{inertia}$	Min.	No virtual inertia is used in this case	-0.000579	-0.000663	-0.000323
	Max.		0.000531	0.000471	0.000245
	Mean		-8.262e^{-07}	-4.006e^{-07}	-1.990e^{-07}
	STD		0.000116	0.000101	4.262e^{-05}
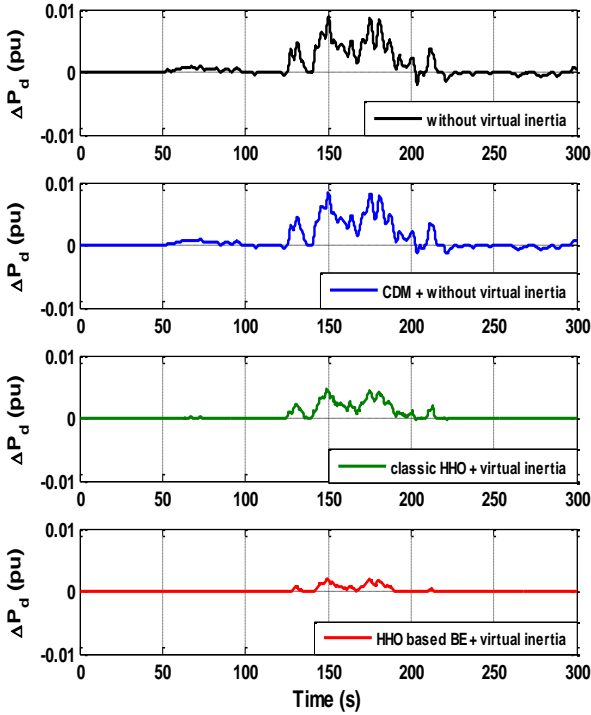
(b) Diesel power change.
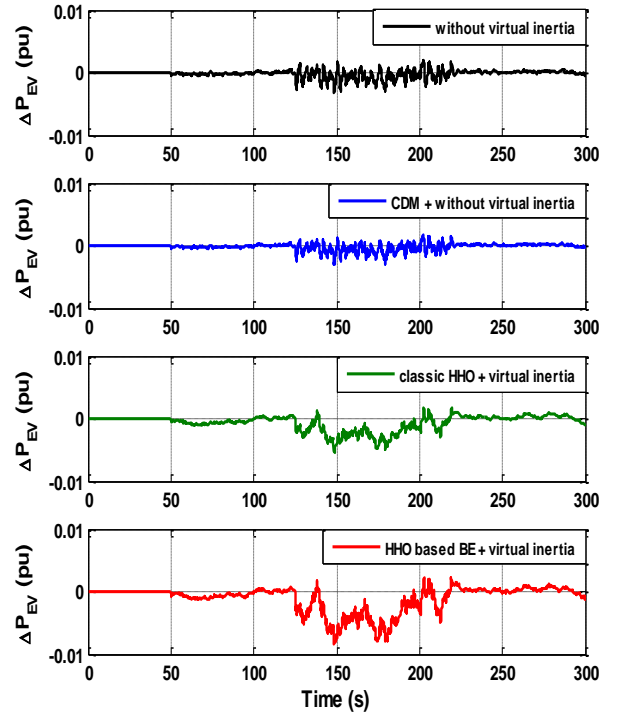
(c) Electric vehicles discharging power.
Fig. 22. System response of case 2 for scenario A.2.
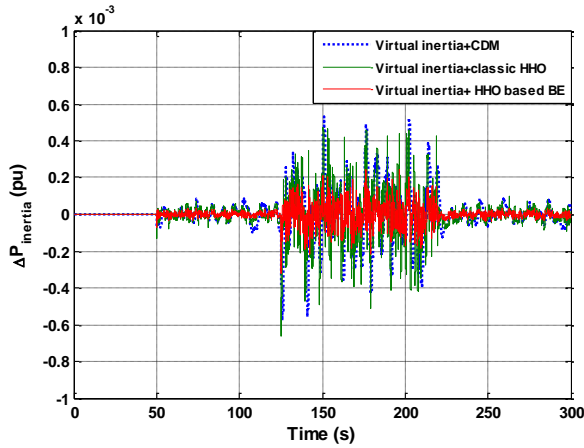
Fig. 23. Power variation of VSG for scenario A.2

Scenario B: Performance evaluation under plug-in/out of EVs.

The system has been examined in multiple operating conditions, it is supposed that $T_{EV1}, T_{EV2}, T_{EV3}, T_{EV4}, T_{EV5}$ as described in first scenario (nominal case), T_g is increased by 40% to .014 sec, T_t is increased to 7 sec. and D is increased by 200% to 0.24 pu.MW/Hz at the moments (t = 950 s). The system is tested in presence of random power fluctuations shown in Fig. 20. In addition, electric vehicles EVs suggested to be plug-in and plug-out the proposed system under the supposed multiple operating conditions as listed in Table 8.

Figure 24 describes the system response for the proposed control strategy for plug-in EVs using adaptive HHO based BE in presence of virtual controller and compared with classic HHO, and CDM controller with /without virtual inertia controller.

Figure 24(a) indicates that the deviation in frequency for CDM without virtual inertia is approximately equals to ± 0.0049 Hz, when added the virtual inertia, it arrives to ± 0.0032 Hz. The deviation Δf changes around ± 0.0024 Hz in case of classic HHO, and while the frequency deviation with suggested with modified HHO based BE supported by virtual inertia controller has been decreased to less than ± 0.001 Hz. This result has supported by Table 9, and it indicates that the system using the proposed adaptive control strategy can gives a desirable performance response as compared to other ones.

Figure 24(b) shows that the required diesel power ΔP_d for the proposed HHO based BE in presence of virtual inertia controller is smaller than those of other one under assumed various operating conditions.

Figure 24(c) shows that how the discharging occurred in the power of EVs by the proposed control schemes, ΔP_{EV} vibrated by a range of 0.014 pu (for a system with virtual inertia + modified HHO based BE), it vibrated by a range of 0.008 pu (for a system with virtual inertia + classic HHO), with a range of 0.0044 pu (for a system with virtual inertia + CDM) and with a range of 0.0052 pu (only CDM without virtual inertia). It is clarified that the discharged power of EVs of the suggested adaptive HHO based BE

controller is higher than those of the other ones. This is a great indication about how larger of power participated with less time at the moment of any abrupt disturbances that happened within the system.

Figure 25 illustrates the interaction between the virtual inertia power change with integration of electric vehicles at the supposed multiple operating conditions. From Table 9, it is clear that the system with modified HHO based BE can decrease the total variation in the power of the virtual inertia as compared to classic HHO and CDM controllers.

Finally, digital simulation results show that the transient performance in case of the proposed adaptive control strategy for plug-in EVs gives better efficiency in damping system oscillations as compared to other controllers in terms of frequency deviation and total power consumption besides using a virtual inertia control. The aforementioned analysis for scenario B has supported by a numerical evidence as shown in Table 8.

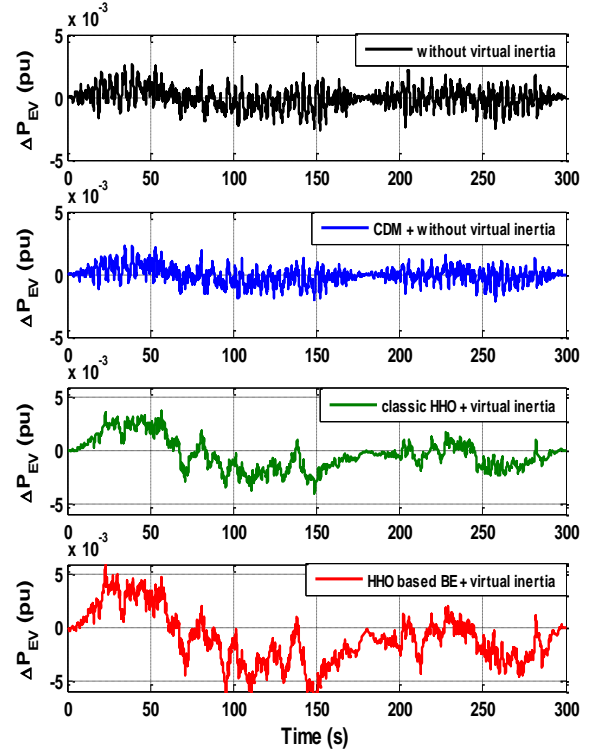**Table 8** Multiple operating conditions of electric vehicle units.

No. of units	Start	Stop	Start	Stop
EV1	45 s	125 s	-	-
EV2	45 s	125 s	210 s	275 s
EV3	-	-	251 s	300 s
EV4	126 s	175 s	-	-
EV5	150 s	175 s	210 s	275 s

(a) Frequency deviation response.

20
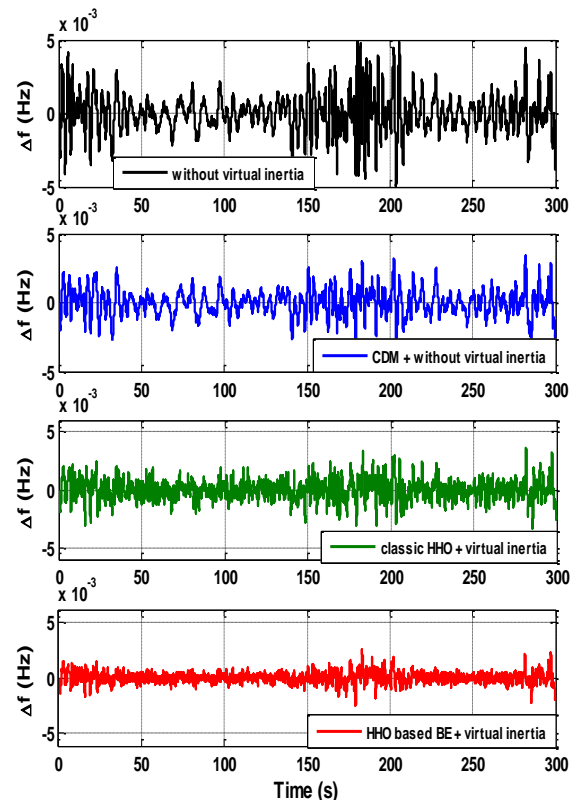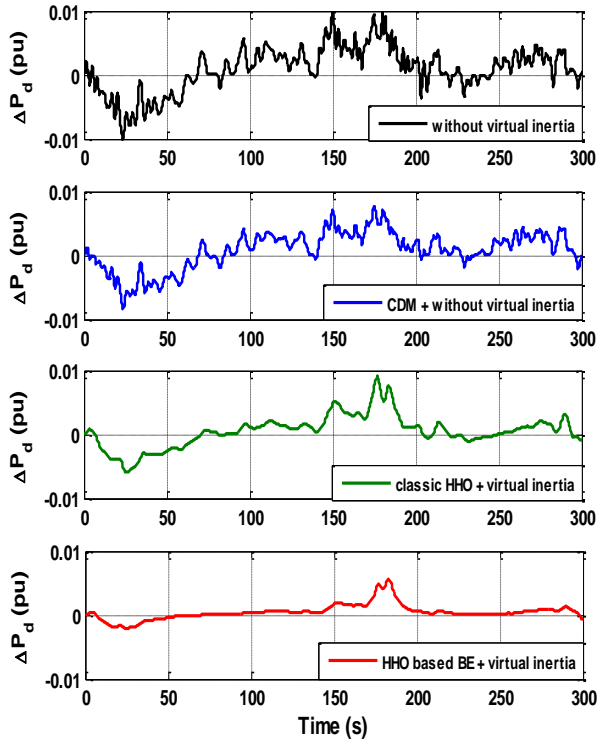
(b) Diesel generator power change.

(c) Discharging power of EVs.

Fig. 24. System response for scenario B.

Table 9 Measurements of the adaptive controllers in case of plug-in/out of electric vehicles (EVs).related to scenario B.

Parameter	Index	CDM without virtual inertia	CDM + virtual inertia	Classic HHO + virtual inertia	HHO based BE + virtual inertia
Δf	Min.	-0.004900	-0.003030	-0.003262	-0.002541
	Max.	0.005209	0.003459	0.003620	0.002590
	Mean	-4.112e^{-06}	-2.935e^{-06}	-2.563e^{-06}	-1.832e^{-06}
	STD	0.001374	0.000955	-0.005945	0.000499
ΔP_d	Min.	-0.010080	-0.008467	0.009020	-0.002067
	Max.	0.009841	0.007677	0.000500	0.005708
	Mean	0.000891	0.000852	0.002536	0.000442
	STD	0.003510	0.002949	0.001061	0.001210
ΔP_{EV}	Min.	-0.002628	-0.002157	-0.004098	-0.007610
	Max.	0.002676	0.002291	0.003803	0.006232
	Mean	-8.341e^{-05}	-8.218e^{-05}	-0.000363	-0.001044
	STD	0.000787	0.000629	0.001491	0.002401
$\Delta P_{inertia}$	Min.	No virtual inertia is used in this case	-0.0007754	-0.0007185	-0.0005127
	Max.		0.0008636	0.0007804	0.0005715
	Mean		2.1760e^{-08}	4.0720e^{-07}	-1.597e^{-07}
	STD		0.0002477	0.0002037	0.0001082
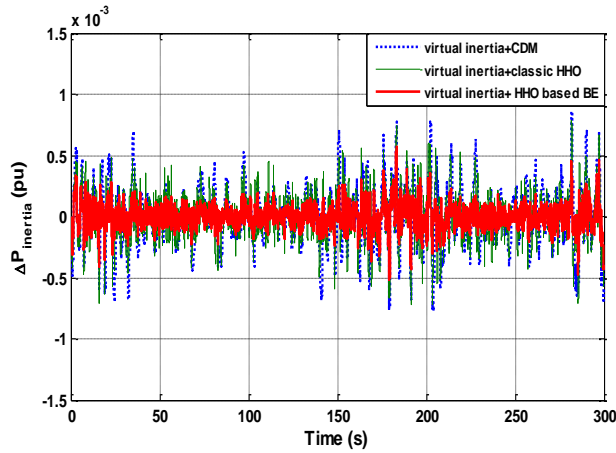
Fig. 25. Power of VSG for scenario B.

10. INTERCONNECTED MULTI- AREA MICROGRID SYSTEM

The suggested control strategy has been extended to interconnect identical two area μG. It is necessary to keep the power of tie-line $\Delta P_{tieline}$ at the scheduled values in addition to restore the system frequency to its desired value for a multi-area power system.

Digital analyses were performed to validate the efficacy of the adaptive control strategy using HHO based BE supported by virtual inertia control loop for plug-in EVs. The nominal data of the suggested two-area μG are described in Table 10 (it is assumed as a single area parameter in section 3.1). The general architecture of the communicated two-area μG is shown in Fig. 26.

The system has been studied and examined along with a generation rate constraint (GRC) equal to 20% per minute under integrations of PVs with charging/discharging of PEVs in presence of virtual inertia control loop. In addition, the communication time delay is assumed to be **1** sec.

10.1. Case study: Performance evaluation under the effect of RESs uncertainties with plug-in/out of EVs.

In this study, a 3-units of EVs (2.38 MW per unit) and 6 MW of PVs have been chosen. The change in tie–line power$\Delta P_{tieline}$ and frequency in two areas $\Delta f_1 and \Delta f_2$ have been tested under the effect of the RESs uncertainties after adding a 6 MW PV to area 1 from 9.00 AM to 15.00 PM as an additional power source with the support of virtual inertia control loop.

Figure 27 shows the change in PV powerΔP_{PV}. In Fig. 28, the deviation in the system frequency for classic HHO and CDM controller reaches an unacceptable value, which leads to system collapse and instability. In contrast, the proposed control strategy (HHO based BE + virtual inertia) provides superior performance when successfully treating this contingency. As a result, this provides strong evidence for the robustness of the proposed control strategy over the

other comparative methods by improving the overall transient μG performance as described in Table 11.

In addition, the power change in the tie-line $\Delta P_{tieline}$ is indicated in Fig. 29. The results support the superiority of the suggested on-line tuned (HHO+BE) controller as compared to standard HHO, CDM controller with/without virtual inertia control loop.
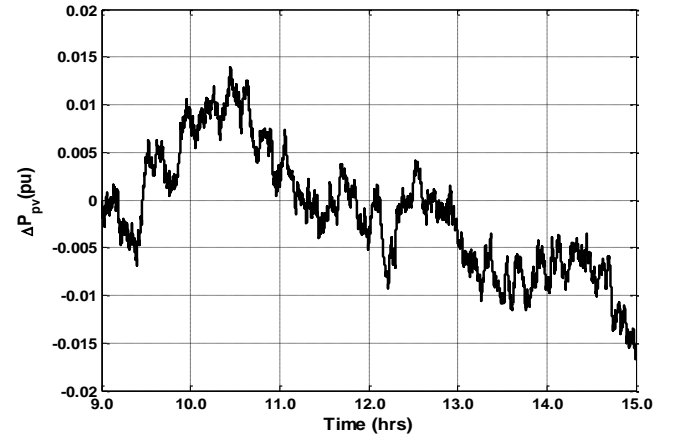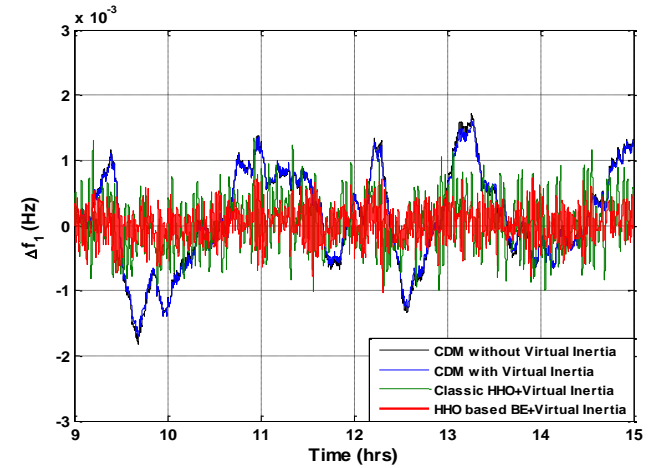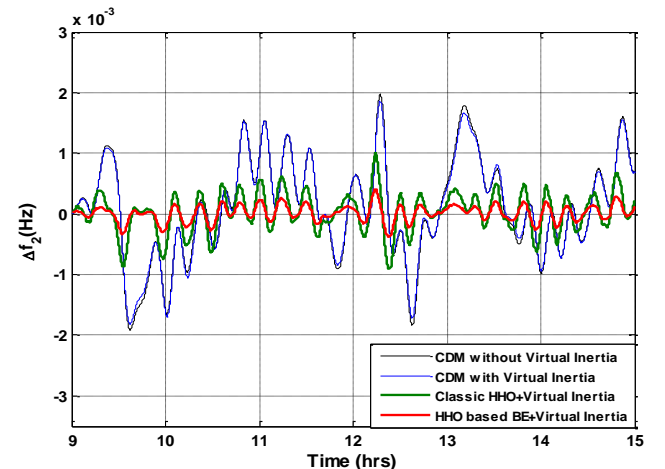

Fig. 27. Change in PV power.

(a)   Frequency deviation response in area 1.

(b)   Frequency deviation response in area 2.
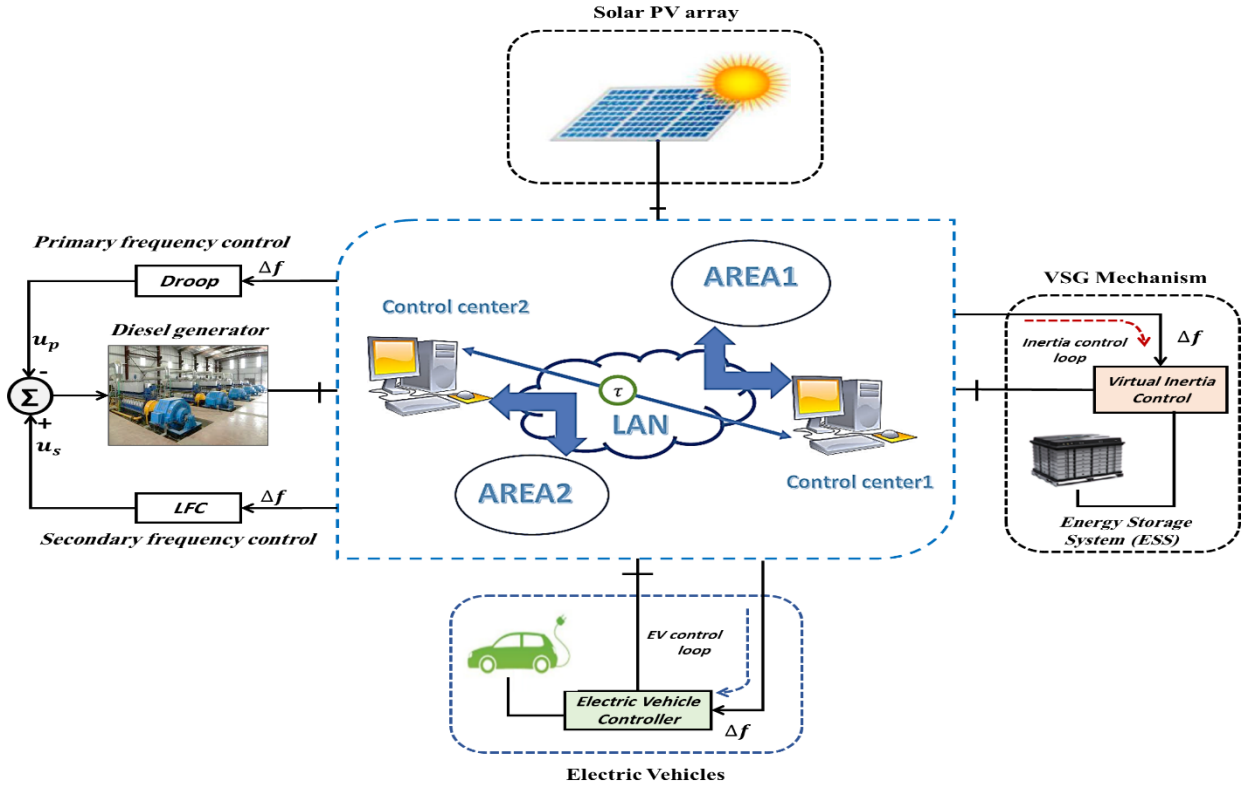**Fig. 28.** System frequency response for two-area μG.

22

Fig. 26. Architecture of interconnected two-area μG.

Table 10 Dynamic Nominal Parameters Of identical interconnected two-area μG system.

Parameter	D_i (pu/Hz)	M_i (pu.sec)	R_i (Hz/pu)	T_{gi} (sec)	T_{ti} (sec)	$T_{inertia,i}$ (sec)	T_{EVi} (sec)	T_{ij} (MW/rad)	β_i (p.u MW/Hz)	GRC (p.u.MW/min)
Area, i	0.12	0.20	2.40	0.10	0.40	10.0	0.28	0.2	0.345	20%

Table 11 Measurements of the adaptive controllers in case of RESs perturbation related to scenario A for two area μG.

Parameter	Index	CDM without virtual inertia	CDM + virtual inertia	Classic HHO + virtual inertia	HHO based BE + virtual inertia
Δf_1	Min.	-0.00182	-0.00171	-0.00102	-0.00103
	Max.	0.00171	0.00162	0.00135	0.00073
	Mean	-0.00012	0.00014	$2.98e^{-05}$	$1.18e^{-05}$
	STD	0.00074	0.00072	0.00041	0.00025
Δf_2	Min.	-0.00191	-0.00181	-0.00091	-0.00038
	Max.	0.00197	0.00187	0.00099	0.00041
	Mean	0.00011	0.00011	$2.73e^{-05}$	$1.08e^{-05}$
	STD	0.00082	0.00080	0.00033	0.00013
$\Delta P_{tie\text{-}line}$	Min.	-0.00066	-0.00064	-0.00041	-0.00018
	Max.	0.00063	0.00060	0.00050	0.00023
	Mean	$-2.84e^{-05}$	$-2.28e^{-05}$	$-3.99e^{-06}$	$-1.65e^{-06}$
	STD	0.00022	0.00022	0.00016	$6.58e^{-05}$
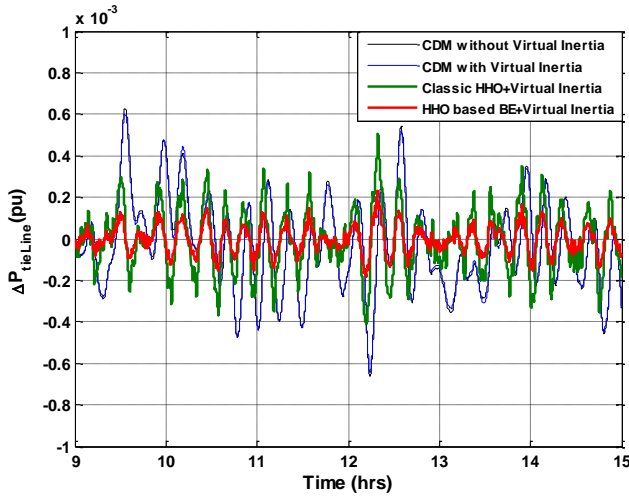
Fig. 29. Change of tie-line Power in scenario A.

CONCLUSION

A new coordination control strategy for plug-in electric vehicle EVs using adaptive HHO based BE in presence of the virtual inertia for an islanded single area and interconnected two area μGs with integrations of RESs and EVs has been presented for enhancement of the frequency stability and preservation of the μG dynamic due to the high penetration level of RESs. LFC is a very important issue in μG system, especially in presence of power fluctuations resulted from RESs that lead to mimic the overall system inertia in the suggested μGs.

In this study, HHO based BE has been investigated for adaptive tuning the integral controller's gains of EVs in μG. Multiple scenarios have introduced to examine the system with the proposed control method (including the case of random load variations, parametric uncertainties and power fluctuations of PV source).

A comparative study of performance between proposed control strategy adjusted by HHO based BE, classic HHO, and CDM was carried out for plug-in EVs in presence of virtual inertia controller. A close results analysis clarified that the proposed strategy (HHO based BE for EVs supported by virtual inertia) can effectively be used to damp out the oscillations in the system, and guarantee robust performance as compared to classic HHO and CDM controller with/without the virtual inertia controller. Thus, the proposed coordination scheme has achieved effective performance to maintain the dynamic stability of μG.

The future chances and challenges will focus on:
- Balloon Effect control method will be re-design and proven in a discrete time system and expanded to stabilize the oscillations in frequency and power with the integration of RESs such as wind energy and PVs and flexible loads such as hybrid electric vehicle (EVs) and heat pumps (HPs) in multi-area interconnected power systems. Additionally, it will be

provided for on-line tuning the VSG controller's parameters.
- The proposed control strategy will be used in the design of the power system stabilizer (PSS) to present the suitable damping characteristics of a synchronous generator when offshore solar concentrated ocean thermal energy conversion system (SC-OTEC) connected to an onshore power grid.

DECLARATION OF COMPETING INTEREST

The authors declare no conflicts of interest in relation to this work.

AUTHOR CONTRIBUTION

Conceived the idea, H. A., and T. H. M..; designed the system modelling, H. A., and T. H. M..; writing the manuscript, H. A.; review and editing the manuscript, J. M. G., G. A-T., and M. M. H.; providing language, J. M. G., and G. A-T. All authors have organized and refined the manuscript.

APPENDIX A

A.1 Solar Irradiation Power

An equivalent (PV) generation plant can represent a solar power generation. Whereas, the power produced by the PV generation system is irregular due to dependence on weather conditions. Consequently, fluctuations of the solar power generation units can be estimated by looking at the deviation from non-uniform and uniform insolation as shown in Fig. A.1.

An accurate output power profile for the solar PV irradiation model can be obtained by modelling the original random output fluctuation using the white noise block in Matlab that multiplied by the standard deviation [40]. The solar power deviation is simulated close to an actual solar power change by the following function:

$$\Delta P_{solar} = 0.6\sqrt{P_{solar}} \qquad (A.1)$$

A.2 Random Load Model

Figure A.2 shows a simplified model for a random load that used in this research. In this model, the load deviation is simulated close to an actual load change by the following function [11]:

$$\Delta P_{load} = 0.6\sqrt{P_{load}} \qquad (A.2)$$

The period of fluctuation is about (5 minutes) according to LFC. White noise block is used to generate the original random variation, to work only during the fluctuation period, a low pass and high filters are used respectively. The output fluctuation has been calculated by multiplying both of the capacity of base load and the standard deviation.
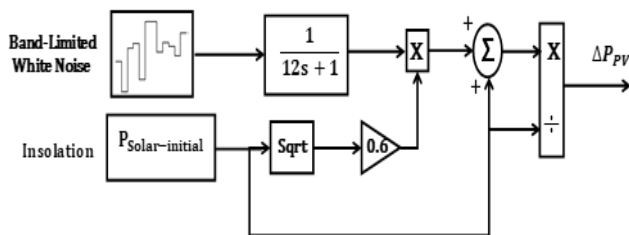

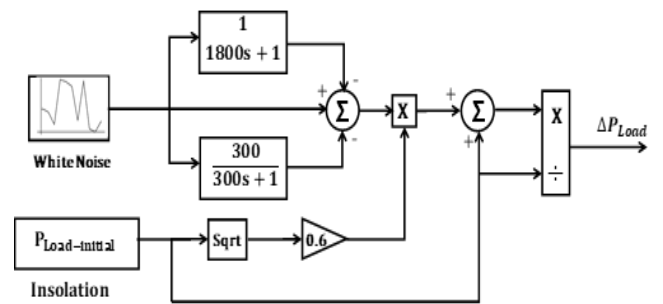**Fig. A.1** PV solar power model using Matlab/Simulink.

Fig. A.2 Random load model using Matlab/Simulink.

REFERENCES

[1] Wu L., Infield D. G. Towards an Assessment of Power System Frequency Support from Wind Plant—Modeling Aggregate Inertial Response," in IEEE Transactions on Power Systems 2013; 28(3), 2283-2291. Available at: doi: 10.1109/TPWRS.2012.2236365.

[2] Hassan B., Toshifumi ISE., Yushi M. Virtual synchronous generators: A survey and new perspectives. International Journal of Electrical Power & Energy Systems 2014; 54: 244-254. Available at: https://doi.org/10.1016/j.ijepes.2013.07.009.

[3] Tamrakar U., Maharjan S. M., Bahattarai B., Hansen T. M., Tonkoski R. Virtual inertia: current trends and future directions. Applied Sciences 2017; 7(7): p. 2–29. Available at: https://doi.org/10.3390/app7070654.

[4] Cheema, K. M. A comprehensive review of virtual synchronous generator. International Journal of Electrical Power & Energy Systems 2020; 120, 106006. https://doi.org/10.1016/j.ijepes.2020.106006

[5] Kerdphol T., Rahman F.S., Mitani Y. Virtual inertia control application to enhance frequency stability of interconnected power systems with high renewable energy penetration. Energies 2018; 11(4): 2–16. Available at: https://doi.org/10.3390/en104981

[6] Kerdphol T., Watanabe M., Hongesombut K., Mitani Y. Self-Adaptive Virtual Inertia Control-Based Fuzzy Logic to Improve Frequency Stability of Microgrid with High Renewable Penetration. In IEEE Access 2019; 7: p. 76071-76083. Available at: doi: 10.1109/ACCESS.2019.2920886.

[7] Kerdphol T., Rahman F.S., Mitani Y., Watanabe. M., Küfeoğlu S. Robust virtual inertia control of an islanded microgrid considering high penetration of renewable energy. IEEE. Access 2018; 6 (1): p. 625–636. Available at: doi: 10.1109/ACCESS.2017.2773486.

[8] Kerdphol T., Rahman F.S., Mitani Y., Hongesombut. K., Küfeoğlu S. Virtual inertia control-based model predictive control for microgrid frequency stabilization considering high renewable energy integration. Sustainability 2017; 9 (5): p. 1–21. Available at: https://doi.org/10.3390/su9050773.

[9] Hou X., Sun Y., Zhang X., Lu J., Wang P., J. M. Guerrero. Improvement of Frequency Regulation in VSG-Based AC Microgrid via Adaptive Virtual Inertia. In IEEE Transactions on Power Electronics 2020; 35(2): p. 1589-1602. Available at:, doi: 10.1109/TPEL.2019.2923734.

[10] Yang D., Jin E., You J., Hua L. Dynamic Frequency Support from a DFIG-Based Wind Turbine Generator via Virtual Inertia Control. Applied Sciences 2020; 10(10),: 3376. Available at : https://doi.org/10.3390/app10103376

[11] Magdy G., Shabib G., Elbaset A. A., Mitani Y. Renewable power systems dynamic security using a new coordination of frequency control strategy based on virtual synchronous generator and digital frequency protection. International Journal of Electrical Power & Energy Systems 2019; 109: p. 351-368. Available at: https://doi.org/10.1016/j.ijepes.2019.02.007

[12] Liu J., Yang Z., Yu J., Huang J., Li W. Coordinated control parameter setting of DFIG wind farms with virtual inertia control. International Journal of Electrical Power & Energy Systems 2020; 122: p. 106167. Available at: https://doi.org/10.1016/j.ijepes.2020.106167

[13] Bahrami S., Amini M. H. A decentralized trading algorithm for an electricity market with generation uncertainty. Appl. Energy 2018; 218 (1): p. 520–532. Available at: https://doi.org/10.1016/j.apenergy.2018.02.157.

[14] Bahrami S., Amini M. H., Shafie-Khah M., Catalao J. P. A decentralized renewable generation management and demand response in power distribution networks. IEEE Transactions on Sustainable Energy2018; 9 (4): p. 1783– 1797. Available at: doi: 10.1109/TSTE.2018.2815502.

[15] Hirase Y., Abe K., Sugimoto K., Sakimoto K., Bevrani H., Ise T. A novel control approach for virtual synchronous generators to suppress frequency and voltage fluctuations in microgrids. Applied Energy 2018; 210: p. 699-710. Available at: https://doi.org/10.1016/j.apenergy.2017.06.058.

[16] Shi R., Zhang X., Hu C., Xu H., Gu J., Cao W. Self-tuning virtual synchronous generator control for improving frequency stability in autonomous photovoltaic-diesel microgrids. Journal of Modern Power Systems and Clean Energy 2018; 6(3): p. 482–494. Available at: https://doi.org/10.1007/s40565-017-0347-3.

[17] Ali R., Mohamed T. H., Qudaih Y. S., Mitani Y. A new load frequency control approach in an isolated small power systems using coefficient diagram method. International Journal of Electrical Power & Energy Systems 2014; 56: p.110-6. Available at: https://doi.org/10.1016/j.ijepes.2013.11.002.

[18] Ali H., Magdy G., Li B., Shabib G., Elbaset A. A., Xu D., Mitani Y. A new frequency control strategy in an islanded microgrid using virtual inertia control-based coefficient diagram method. IEEE Access 2019; 7: p. 16979-16990. Available at: doi:10.1109/ACCESS.2019.2894840

[19] Manabe S. Importance of coefficient diagram in polynomial method. Decision and Control, Proceedings 42nd IEEE Conference on: IEEE 2003; p. 3489-94. Available at: 10.1109/CDC.2003.1271687

[20] Richardson. D. B. Electric vehicles and the electric grid: A review of modeling approaches, Impacts, and renewable energy integration. Renewable and Sustainable Energy Reviews 2013; 19, p. 247-254. Available at: doi: https://doi.org/10.1016/j.rser.2012.11.042

[21] Wu. X., Hu. X., Yin. X., Moura. S. J. Stochastic optimal energy management of smart home with PEV energy storage. IEEE Transactions on Smart Grid 2016; 9(3): p. 2065-2075. Available at: doi: 10.1109/TSG.2016.2606442.

[22] Wu. X., Hu. X., Teng. Y., Qian. S., Cheng. R. Optimal integration of a hybrid solar-battery power source into smart home nanogrid with plug-in electric vehicle. Journal of power sources 2017; 363:, p. 277-283. Available at: https://doi.org/10.1016/j.jpowsour.2017.07.086.

[23] Islam. M. S., Mithulananthan. N., Hung. D. Q. Coordinated EV charging for correlated EV and grid loads and PV output using a novel, correlated, probabilistic model. International Journal of Electrical Power & Energy Systems 2019; 104: p. 335-348. Available at: https://doi.org/10.1016/j.ijepes.2018.07.002

[24] Xu H., Miao S., Zhang C., Shi D. Optimal placement of charging infrastructures for large-scale integration of pure electric vehicles into grid. International Journal of Electrical Power &Energy System 2013; 53: p. 159-165. Available at: https://doi.org/10.1016/j.ijepes.2013.04.022.

[25] Khooban M. H., Niknam T., Blaabjerg F., et al. A new load frequency control strategy for micro-grids with considering electrical vehicles. Electr. Power Syst. Res. 2017; 143 (1): p. 585–598. Available at: https://doi.org/10.1016/jepsr.2016.10.57.

[26] H. M. Hasanien, A. A. El-Fergany. Salp swarm algorithm-based optimal load frequency control of hybrid renewable power systems with communication delay and excitation cross-coupling effect. Electric Power Systems Research 2019; 176: p. 105938. Available at: https://doi.org/10.1016/j.epsr.2019.105938

[27] Wang. W., Chen. P., Zeng. D. and Liu. J. Electric Vehicle Fleet Integration in a Virtual Power Plant With Large-Scale Wind Power. In IEEE Transactions on Industry Applications 2020; 56(5): p. 5924-5931. Available at: 10.1109/TIA.2020.2993529.

[28] Sahu R. K., Panda S., Padhan S. A hybrid firefly algorithm and pattern search technique for automatic generation control of multi area power systems. International Journal of Electrical Power & Energy Systems 2015; 64: p. 9-23. Available at: https://doi.org/10.1016/j.ijepes.2014.07.013.

[29] Sahu B. K., Pati T. K., Nayak J. R., Panda S., and Kar S. K. Anovel hybrid LUS_TLBO optimized fuzzy-PID controller for load frequency control of multi-source power system. International Journal of Electrical Power & Energy Systems. 2016; 74: p. 58-69. Available at: https://doi.org/10.1016/j.ijepes.2015.07.020

[30] Sambariya D. K., Shrangi S. Optimal design of PID controller for load frequency control using harmony search algorithm. Indonesian Journal of Electrical Engineering and Computer Science 2017; 5(1): p. 19. Available at: 10.11591/ijeecs.v5.i1.pp19-32 [Cross Reference].

[31] Abd-Elazim S. Ali E. Load frequency controller design via BAT algorithm for nonlinear interconnected power system. International Journal of Electrical Power & Energy Systems 2016; 77: p. 166-177. Available at: https://doi.org/10.1016/j.ijepes.2015.11.029.

[32] Bošković M. Č., Tomislav B. Š., Milan R. R. Novel tuning rules for PIDC and PID load frequency controllers considering robustness and sensitivity to measurement noise. International Journal of Electrical Power & Energy Systems 2020; (114:105416. Available at: https://doi.org/10.1016/j.ijepes.2019.105416.

[33] Bevrani H., Hiyama T. On load_frequency regulation with time delays: Design and real-time implementation. IEEE transactions on energy conversion 2009; 24(1): p. 292-300. Available at: doi: 10.1109/TEC.2008.2003205

[34] Naidu K., Mokhlis H., Bakar A., Terzija V., Illias H. Application of firefly algorithm with online wavelet filter in automatic generation

control of an interconnected reheat thermal power system International Journal of Electrical Power & Energy Systems 2014; 63: p. 401-413. Available at: https://doi.org/10.1016/j.ijepes.2014.05.055.

[35] Fini M. H., Youse G. R., Alhelou H. H. Comparative study on the performance of many-objective and single-objective optimization algorithms in tuning load frequency controllers of multi-area power systems. IET Generation, Transmission & Distribution 2016; 10(12): p. 2915-2923. Available at: http://dx.doi.org/10.1049/iet-gtd.2015.1334

[36] Hussein A., Mahmoud M. H., Tarek H. M. Frequency Stabilization of Two Area Power System Interconnected by AC/DC Links using Jaya Algorithm. In international of Journal Advanced Science and Technology 2020; 29(1): p. 548-559. Available at: http://sersc.org/journals/IJAST/3279.

[37] Abubakr H., Mohamed T. H., Hussein M. M., Shabib, G. Adaptive Frequency Regulation in Interconnected Two Area Microgrid System. In 2019 IEEE Conference on Power Electronics and Renewable Energy (CPERE) 2019; p. 284-289. Available at: doi: 10.1109/CPERE45374.2019.8980188.

[38] Heidari A. A., Mirjalili S., Faris H., Aljarah I., Mafarja M., Chen H. Harris hawks optimization: Algorithm and applications. Future generation computer systems 2019; 97: p. 849-872. Available at: https://doi.org/10.1016/j.future.2019.02.028.

[39] Mohamed, T. H., Abubakr, H., Alamin, M. A. M., Hassan, A. M. Modified WCA based Adaptive Control Approach Using Balloon Effect: Electrical Systems Applications. IEEE Access 2020; 8(1), p. 60877-60889. Available at: doi: 10.1109/ACCESS.2020.2982510.

[40] Dahab Y. A., Abubakr H., and Mohamed T. H. Adaptive Load Frequency Control of Power Systems Using Electro-Search Optimization Supported by the Balloon Effect. IEEE access 2020; 8: p. 7408-7422. Available at: 10.1109/ACCESS.2020.2964104.

[41] Tarek H. M., Mohamed A. M. A., Ammar M. H. Adaptive position control of a cart moved by a DC motor using integral controller tuned by Jaya optimization with Balloon effect. Computers and Electrical Engineering 2020; 87: p. 106786. Available at: https://doi.org/10.1016/j.compeleceng.2020.106786.

[42] Teimourzadeh S., Aminifar F., Davarpanah M. Microgrid dynamic security: challenges, solutions, and key considerations. The Electricity Journal 2017; 30 (1): p. 43–51. Available at: https://doi.org/10.1016/j.tej.2017.04.015.

[43] Zhang. Q., Li. Y., Ding. Z., Xie. W., and Li. C. Self-Adaptive Secondary Frequency Regulation Strategy of Micro-Grid with Multiple Virtual Synchronous Generators. IEEE Transactions on Industry Applications 2020; 56(5): p.6018 – 6007 . Available at: doi: 10.1109/TIA.2020.2975144

[44] Bevrani H., Francois B., Ise T. Microgrid dynamics and control. John Wiley& Sons, Hoboken, NJ, USA, 2017.

[45] Zhang. Q., Li. Y., Li. C., and Li. C., Grid frequency regulation strategy considering individual driving demand of electric vehicle. Electric Power Systems Research 2018; 163: p. 38-48. Available at: https://doi.org/10.1016/j.epsr.2018.05.019.

[46] Zhang. Q., Liu. H., and Li, C. A hierarchical dispatch model for optimizing real-time charging and discharging strategy of electric vehicles. IEEJ Transactions on Electrical and Electronic Engineering 2018; 13(4): p. 537-548. Available at: https://doi.org/10.1002/tee.22599.

[47] Abubakr H., Mohamed T. H., Hussein M. M., Shabib G. ESO-Based Self Tuning Frequency Control Design for Isolated Microgrid System. In: 21st International Middle East Power Systems Conference (MEPCON), Cairo, Egypt 2019; p. 589-593. Available at: doi:10.1109/MEPCON47431.2019.9008042

[48] Sastry S., Bodson M. Adaptive control: stability, convergence and robustness. Courier Corporation 2011;

[49] Bhushan B., Singh M. Adaptive control of DC motor using bacterial foraging algorithm. Applied Soft Computing 2011; 11(8): p. 4913–4920. Available at: https://doi.org/10.1016/j.asoc.2011.06.008.